Received 2013 September 30; accepted 2014 July 4
Preprint typeset using LaTeX style emulateapj v. 5/2/11

arXiv:1407.6717v1 [astro-ph.HE] 24 Jul 2014

AN *XMM-Newton* STUDY OF THE MIXED-MORPHOLOGY SUPERNOVA REMNANT W28 (G6.4−0.1)

Ping Zhou[1,2], Samar Safi-Harb[2,4], Yang Chen[1,3], Xiao Zhang[1], Bing Jiang[1], and Gilles Ferrand[2]
[1]School of Astronomy and Space Science, Nanjing University, Nanjing 210093, China
[2]Department of Physics and Astronomy, University of Manitoba, Winnipeg R3T 2N2, Canada
[3] Key Laboratory of Modern Astronomy and Astrophysics, Nanjing University, Ministry of Education, China
Received 2013 September 30; accepted 2014 July 4

ABSTRACT

We have performed an *XMM-Newton* imaging and spectroscopic study of supernova remnant (SNR) W28, a prototype mixed-morphology or thermal composite SNR believed to be interacting with a molecular cloud. The observed hot X-ray emitting plasma is characterized by low metal abundances, showing no evidence of ejecta. The X-rays arising from the deformed northeast shell consist of a thermal component with a temperature of ~ 0.3 keV plus a hard component of either thermal (temperature ~ 0.6 keV) or non-thermal (photon index = 0.9–2.4) origin. The X-ray emission in the SNR interior is blobby and the corresponding spectra are best described as the emission from a cold ($kT \sim 0.4$ keV) plasma in non-equilibrium ionization with an ionization timescale of $\sim 4.3 \times 10^{11}$ cm^{-3} s plus a hot ($kT \sim 0.8$ keV) gas in collisional ionization equilibrium. Applying the two-temperature model to the smaller central regions, we find non-uniform interstellar absorption, temperature and density distribution, which indicates that the remnant is evolving in a non-uniform environment with denser material in the east and north. The cloudlet evaporation mechanism can essentially explain the properties of the X-ray emission in the center and thermal conduction may also play a role for length scales comparable to the remnant radius. A recombining plasma model with an electron temperature of ~ 0.6 keV is also feasible for describing the hot central gas with the recombination age of the gas estimated at $\sim 2.9 \times 10^4$ yr.

Subject headings: cosmic rays —ISM: individual (G6.4−0.1 = W28) — ISM: supernova remnants — radiation mechanisms: nonthermal — radiation mechanisms: thermal

1. INTRODUCTION

Mixed-morphology (MM) or thermal composite supernova remnants (SNRs) represent a class of SNRs which consist of thermal X-ray-filled centers and radio-bright shells, such as W44, W28, 3C391, and W49B (Rho & Petre 1998; Jones et al. 1998). This category of SNRs displays a good correlation with H I or molecular clouds (MCs; Rho & Petre 1998; also see the SNR–MC association catalog in Jiang et al. 2010) and shows a strong association with 1720 MHz OH masers (Green et al. 1997; Yusef-Zadeh et al. 2003). The MM SNRs have received two decades of studies since the standard Sedov (1959) evolution fails to predict their centrally peaked X-ray morphology. Debates on the origin of the central X-rays are still on-going. Several competitive scenarios were proposed to explain the bright X-ray emission in the MM SNR interior. The first one invokes the thermal conduction model leading to a central density increase (Cui & Cox 1992; Shelton et al. 1999; Cox et al. 1999). It predicts that the temperature smoothly decreases while the density rises away from the center, creating a "center-filled" hot X-ray morphology with a thin, dense, and cold radiative shell in the periphery. The second scenario is the cloudlet evaporation model (White & Long 1991). In this model, ambient cloudlets engulfed by the SNR shock gradually evaporate into the hot gas, resulting in an increased density in the SNR interior.

Recent *Suzaku* observations of a handful MM SNRs (IC443, W49B, G359.1−0.5) have detected strong radiative recombination continua (RRCs), giving the first direct evidence of over-ionization in SNRs (Yamaguchi et al. 2009; Ozawa et al. 2009; Ohnishi et al. 2011). In these SNRs, the ionization temperature kT_z has been found to be significantly higher than the electron temperature kT. As for the origin of the recombining plasma, Itoh & Masai (1989) discussed the rapid electron cooling caused by the rarefaction process after the shock breaks out of the dense circumstellar medium to the rarefied ambient medium. Kawasaki et al. (2002) proposed thermal conduction as a mechanism to produce the over-ionized plasma. Zhou et al. (2011) used a two-dimensional model to investigate SNRs evolving in a ring-like cloud and found that the thermal conduction and the rapid adiabatic expansion are two classes of processes both responsible for the over-ionized plasma in W49B.

In the γ-ray band, a new generation of telescopes such as the High-Energy Stereoscopic System (H.E.S.S) and *Fermi* detected many new SNR–γ-ray associations (Ferrand & Safi-Harb 2012[5] and references therein), providing the best database for studying cosmic rays acceleration in SNRs to the very high energy (VHE) band. Although distinguishing the hadronic γ-ray emission from the leptonic emission is still an on-going effort, accumulating evidence has pointed to SNRs interacting with MCs emitting hadronic γ-rays via proton–proton collision (such as W28, IC443, W51C; Abdo et al. 2009, 2010; Li & Chen 2012). MM SNRs are ideal sites to study hadronic cosmic rays in the VHE band due to its good correlation with the 1720 MHz OH masers, as the masers are considered to be new potential trac-

[4] Canada Research Chair

[5] http://www.physics.umanitoba.ca/snr/SNRcat

ers for the sites with hadronic particle acceleration (Hewitt et al. 2009; Frail 2011). Furthermore, in terms of statistics, recent *Fermi*-LAT observations have revealed that MM SNRs occupy a considerable percentage of the γ-ray-bright SNRs within middle-age (Hewitt & Fermi LAT Collaboration 2012) and most of those MM SNRs likely/probably emit γ-rays via the hadronic process (Brandt & Fermi LAT Collaboration 2012).

Cosmic ray interactions with a dense medium can generate non-thermal radiation in a broad band. Several models have been established to predict the broad band spectrum in MC–SNR interaction sites (e.g. Bykov et al. 2000; Gabici et al. 2009). However, non-thermal X-ray studies of SNRs in the γ-ray-bright and MC–SNR interaction sites are still limited. MM SNRs, especially those bright in both X-ray and γ-ray bands, are good candidates to explore the non-thermal X-ray emission.

W28 (G6.4−0.1) is an evolved SNR, with an estimated age 3.3–4.2 $\times$ 10^4 yr (Rho & Borkowski 2002, hereafter RB02; Velázquez et al.2002; Li & Chen 2010) at a distance of about 2 kpc (Ilovaisky & Lequex 1972; Goudis 1976; Velázquez et al. 2002). It is a well-known MM SNR with double radio shells in its northern hemisphere and a breakout morphology in its southwest (RB02). The interaction of the MCs with the blast wave of the SNR has been studied for 30 yr. Wootten (1981) firstly found broadenings of CO and HCO^+ lines in the northeastern (NE) MC and suggested the cloud is compressed and heated by the W28 shock. The interaction was confirmed with the detections of 1720 OH masers in the NE MC and the cloud on the inner radio shell (Frail et al. 1994; Claussen et al. 1997). Follow-up (sub)millimeter and infrared observations toward the SNR (Arikawa et al. 1999; Reach et al. 2005; Nicholas et al. 2012) gave further evidence for the MC–SNR interaction, and provided detailed physical properties of the smaller clumps embedded in the MCs.

As a prominent γ-ray-emitting SNR, W28 was detected at energy $>$ 300 MeV by COS-B (Pollock 1985), $>$ 100 MeV by EGRET (Sturner & Dermer 1995; Hartman et al. 1999), $>$ 400 MeV by *AGILE* (Giuliani et al. 2010), $>$ 0.2 GeV by Fermi (Abdo et al. 2010), and $>$ 0.1 TeV by H.E.S.S (Aharonian et al. 2008). The GeV–TeV γ-rays are considered to be produced by hadronic interaction of cosmic rays with the NE MCs (Aharonian et al. 2008; Abdo et al. 2010; Li & Chen 2010; Ohira et al. 2011; Yan et al. 2012).

In the X-ray band, W28 has been observed with several generations of X-ray satellites, however, inconsistent spectral results have been obtained. Early *Einstein* IPC + MPC analysis has shown that W28 is a composite SNR and a single thermal component was used to characterize the X-ray emission (Long et al. 1991). The *Chandra* X-ray imaging revealed a bright knotty region in the SNR interior (Keohane et al. 2005). Combining the observations of *ROSAT* and *ASCA*, RB02 showed that a two-thermal-component model (with temperatures of 0.6 and 1.8 keV) is required to reproduce the global X-ray spectrum from the SNR center. This conclusion was also supported by a subsequent *ASCA* study (Kawasaki et al. 2005; hereafter KO05), which searched for evidence of over-ionized plasma but without a successful detection. However, a most recent *Suzaku* analysis disfavored the presence of the hot (1.8 keV) plasma and argued that the central X-rays are emitted by recombining plasma with an electron temperature $\sim$ 0.4 keV (Sawada & Koyama 2012; hereafter SK12). Hence, the nature of the central X-ray emission of W28 is still controversial.

Furthermore, for the NE shell where γ-ray emission has been detected, there is debate on the nature of its X-ray emission, in particular whether there is any non-thermal component or not. RB02 applied a thermal component (0.56 keV) to characterize the X-ray spectrum observed with *ROSAT* and *ASCA*, while Ueno et al. (2003) described the X-ray emission by a two-component model consisting of a cold (kT $\sim$ 0.3 keV) thermal plasma and a very hard (Γ = $1.3^{+0.6}_{-0.9}$) non-thermal tail (*apec* + *powerlaw*) using an 18 ks EPIC pn observation with *XMM-Newton*. Testing the existence of the non-thermal X-ray emission and investigating its origin is essential, because X-rays are in the lower neighboring energy band of γ-rays, and thus provide precious information for the broad-band study of cosmic ray acceleration in SNRs.

Motivated by the inconsistent X-ray results previously obtained with different telescopes, the need to verify and study the non-thermal emission and to search for any spatial variations of the physical properties across W28, we here present our X-ray analysis based on *XMM-Newton* observations. In Section 2, we describe the observations and the data calibration. Section 3 shows the X-ray image and the spatially resolved spectroscopic results. In Section 4, we discuss the physical properties of the hot gas inside W28 with a comparison to previous X-ray studies, and the origin of the non-thermal X-ray emission detected in the NE shell. The conclusions are summarized in Section 5.

2. OBSERVATIONS AND DATA REDUCTION

Four *XMM-Newton* observations toward the SNR W28 were performed in three pointings and cover the northern hemisphere of the remnant. Two observations of the NE shell were carried out on 2002 September 23 and on 2003 October 7–8, respectively, in full frame mode and with thick filter (PI: K. Koyama). Another two archival observations pointing to the center and north of W28 were obtained from the observations toward the Galactic ridge, which were made on 2003 March 19–20 and 2003 March 20, respectively, in full frame mode and with medium filter (PI: R. Warwick). Detailed information of the *XMM-Newton* data, including the coordinates and the effective exposure times (after removing time intervals with heavy proton flarings) of MOS (Turner et al. 2001) and pn (Strüder et al. 2001) for the NE shell, SNR center, and northern region are summarized in Table 1. The Science Analysis System software (SAS,[6] ver. 11.0) was used to reprocess the EPIC data.

3. RESULTS

3.1. *X-ray image*

From the available *XMM-Newton* data, we generated a two-color (0.3–1.0 keV in red and 1.0–7.0 keV in blue) energy map covering the northern hemisphere of W28, overlaid with 1.4 GHz radio contours (as shown in Figure 1(a)). Each of the images in the two bands

[6] http://xmm.esac.esa.int/sas/

TABLE 1
SUMMARY OF THE *XMM-Newton* OBSERVATIONS OF THE SNR W28

Pointing	Obs. ID	Obs. Date	Center (J2000)		Exposure[a] (ks)	
			R.A.	Decl.	MOS	pn
Center	0135742201	2003 Mar 19–20	18:00:21.1	−23:20:19.0	5	4
North	0135742501	2003 Mar 20	18:01:04.3	−23:02:57.0	1	1
Northeast	0145970101	2002 Sep 23	18:01:45.0	−23:18:00.0	21	15
Northeast	0145970401	2003 Oct 7–8	18:01:45.0	−23:18:00.0	9	9

[a] Effective exposure time.

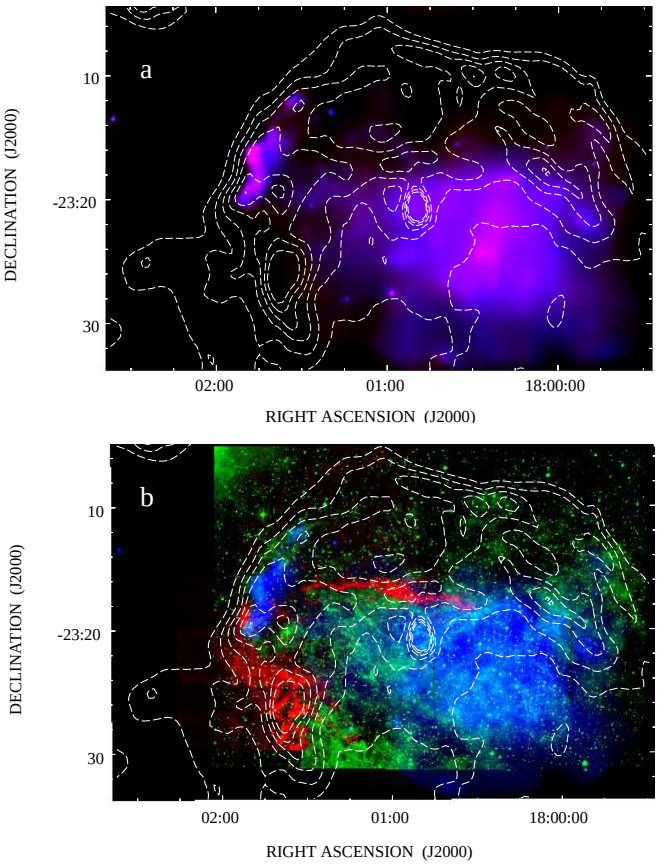

FIG. 1.— (a) *XMM-Newton* EPIC color image of the SNR W28, with red and blue colors corresponding to the 0.3–1.0 keV and 1.0–7.0 keV bands, respectively. Radio contours are overlaid using VLA 1.4 GHz continuum emission with levels of 0.1, 0.22, 0.34, 0.46, 0.58, 0.7 Jy beam^{-1}. (b) Tri-color image of the SNR W28. Red: the intensity map of JCMT ^{12}CO J=3–2 integrated from −40 km s^{-1} to 40 km s^{-1} (Arikawa et al. 1999); green: the narrow-band Hα image obtained from the archival SuperCOSMOS Hα Survey (Parker et al. 2005); and blue: *XMM-Newton* 0.3–7.0 keV X-ray map. The 1.4 GHz radio contours are shown with the same levels as those in panel a.

was exposure-corrected and adaptively smoothed (using "csmooth" command in CIAO[7] 4.3) with a Gaussian kernel σ to achieve a minimum and maximum significance of 3 and 4, respectively.

The brightest X-ray emission arises from the NE shell and the central region as delineated by the inner radio shell. Fainter and diffuse X-ray emission is also seen in the gap between the two radio shells. A section of the radio shell in the northwestern edge is partially X-ray brightened. On the NE shell, an X-ray slab appears distorted and in general bearing a morphological resemblance to the radio brightness peak. The hot gas in the SNR interior appears blobby rather than homogeneous, which is also consistent with the clumpy nature suggested by the *Chandra* imaging study (Keohane et al. 2005).

3.2. *The environmental gas*

We produce a tri-color image of the northern hemisphere of W28, illustrating the ^{12}CO J=3–2 (red), Hα (green), and the X-ray (blue) morphology of W28, overlaid with the radio contours, for comparison (see Figure 1(b). The figure shows that W28 is evolving in a complicated environment with a dense MC in the east and a molecular stripe on the northern inner shell. There is a range of temperature and density distribution on the shells, represented by three kinds of emission: cold and dense MCs indicated by CO emission located in the outermost boundary; hot and tenuous X-rays generally located behind; warm and moderately dense gas radiating Hα emission and situated between the MCs and the X-ray-emitting gas.

The SNR interior filled by X-rays is also bright in diffuse, nonuniform Hα emission, whereas filamentary Hα structures are mostly aligned with the inner radio shell or distributed in the east. The Hα filaments inside the SNR, in addition to the boundary of the diffuse Hα emission in the south and west, appear to confine the central bright X-rays.

3.3. *XMM-Newton Spectral Analysis*

Prior to the extraction of spectra, we removed the point-like sources detected in the extraction regions from the events files. For the three observations pointing to the northeast and center of the remnant, we applied a combination of source detection algorithms (wavelet, sliding-box, and maximum likelihood centroid fitting) described in Wang et al. (2003). For the Galactic ridge observation pointing to the north of the remnant (Obs. ID: 0135742501) which with a short exposure ($\sim$ 1 ks), we detected point-like sources with the SAS edetect_chain script and used a subtraction radius of 0.6′.

We defined two large regions ("Shell" and "C") covering the NE shell and central gas, respectively, to investigate the mean physical characteristics of the two regions with high statistics, and seven small regions ("S1", "S2", "CN", "C1", "C2", "C3", "C4"[8]) along the outer shell and inside the SNR to search for spectral variation (see Figure 2). The extraction of the background spectra

[7] http://cxc.harvard.edu/ciao/

[8] The region "C4" is in the field of the observation pointing to the SNR center and is also covered by MOS1 of the two NE observations.

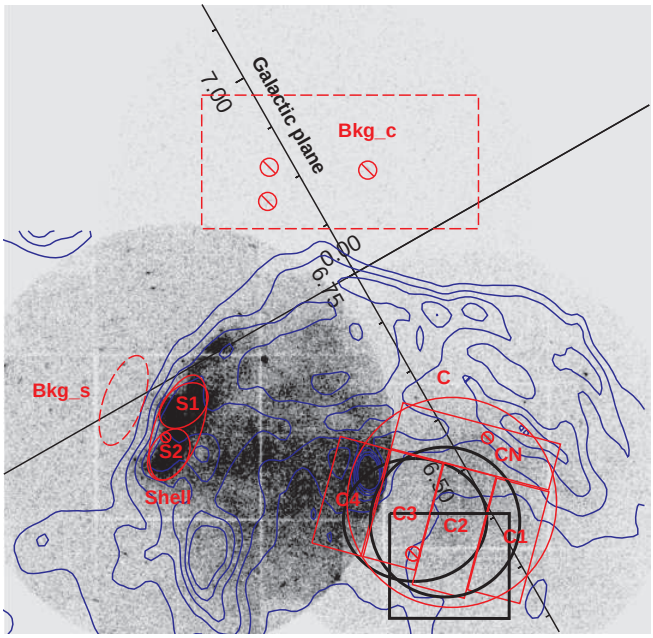

FIG. 2.— *XMM-Newton* raw image of W28 overlaid with radio contours (at the same levels as those in Figure 1(a)). The thin solid and dashed regions colored in red correspond to source and background spectral extraction regions of *XMM-Newton* data. The background spectra for the NE and central observations are extracted separately from the dashed ellipse and northern rectangle. The thin solid circle ("C") in red covers an area that coincides with that chosen by RB02 for spectral analysis of the central gas. The thick black rectangle and ellipse indicate the spectral extraction regions of the "center" and "east" region, respectively, in KO05. The spectral extraction region in SK12 is shown with the thick black circle. The location of the Galactic plane is also shown.

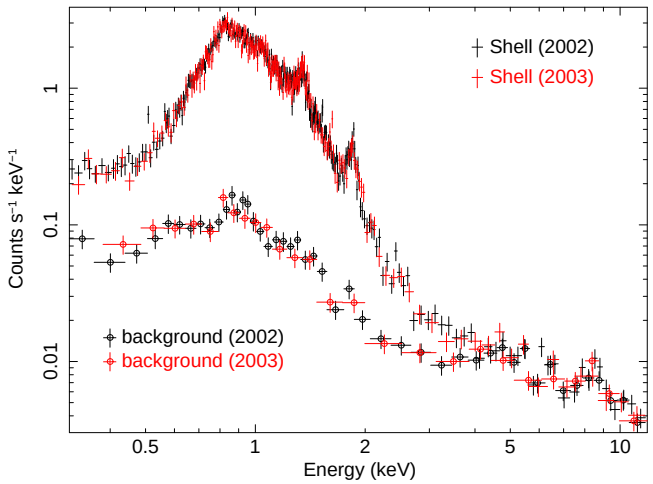

FIG. 3.— EPIC-pn spectra of region "Shell" without background subtraction (dots with error bars) and the normalized background (circles with error bars). We colored the 2002 (Obs ID: 0145970101) and 2003 (Obs ID: 0145970401) data in black and red, respectively. Each spectrum is grouped with a minimum of 40 counts per bin. The background-subtracted spectra are shown in Figure 4.

is described in Section 3.3.1. Each individual spectrum is adaptively binned to achieve a background-subtracted signal-to-noise ratio (S/N) of 3, except that the spectra shown in Figure 3 are grouped to achieve a minimum of 40 counts per bin.

The *vmekal*, *vnei*, and *powerlaw* models in the XSPEC[9] package (ver. 12.7) and the *neij* model in the SPEX software (ver. 2.03.03; Kaastra et al. 1996) were used for spectral fitting (see Sections 3.3.2 and 3.3.3 for detailed description of the models). The spectra of EPIC MOS1, MOS2 and pn from all available observations are jointly fitted together for the individual regions to better constrain the physical parameters.

3.3.1. *Background Subtraction*

W28 is an extended object ($\sim 50'$ in diameter) located in the Galactic plane and close to the Galactic center, where the X-ray emission from the SNR suffers contamination from a high Galactic X-ray background (SK12). Different background regions were selected in the previous *ASCA* and *Suzaku* studies and inconsistent results were obtained (see Figure 2 for the spectral extraction regions used in this study and by RB02, KO05 and SK12). In Section 4.2 below we provide a detailed comparison between the earlier studies and our study. An appropriate background selection is therefore crucial, especially for a reliable study of the central gas that is more than $14'$ away from the northern boundary.

Accordingly, we defined two separate background regions, "Bkg_s" and "Bkg_c" (see Figure 2), for each of the NE observations and the central observation of W28, respectively. Region "Bkg_s" was selected as close as possible to the NE shell and outside the remnant's radio boundary.[10] As the field of view of the *XMM-Newton* observation toward the SNR center (Obs. ID: 0135742201) is almost filled by the remnant, we do not find a proper background region from the same observation. Therefore, "Bkg_c" is selected from a nearby observation (Obs. ID: 0135742501), which pointed to the *same* Galactic latitude as the central gas and was fortunately performed with the same telescope configuration one day afterward. Region "Bkg_c" is the closest background to the remnant and the most appropriate one to minimize any contamination from the Galactic ridge.

3.3.2. *Northeastern Shell*

W28 is a distinct MM SNR partly due to its bright, deformed X-ray shell along the NE boundary. Figure 3 shows the pn spectra extracted from the region "Shell" and its nearby background (normalized by area). The X-ray spectra of the shell show several line features, such as Mg Heα ($\sim$ 1.35 keV), Si Heα ($\sim$ 1.86 keV), and S Heα ($\sim$ 2.45 keV), supporting a thermal plasma origin for at least part of the X-ray emission. The shell X-ray emission extends up to 5 keV, while the background dominates the emission above 5 keV.

Figure 4 shows the EPIC (MOS+pn) background-subtracted spectra of the shell. Adopting the cross-sections from Morrison & McCammon (1983) for the foreground absorption, an absorbed single collisional ionization equilibrium (CIE) model, *vmekal*, and an absorbed non-equilibrium ionization (NEI) model, *vnei* in

[9] http://xspec.gsfc.nasa.gov

[10] Region "Bkg_s" was selected on the same MOS's central CCDs that also cover the source region "Shell" to ensure "Bkg_s" has similar sky and instrumental background to that of the shell regions. The vignetting effect is not expected to be important for the shell considering that "Bkg_s" is adjacent ($4'$) to the "Shell".

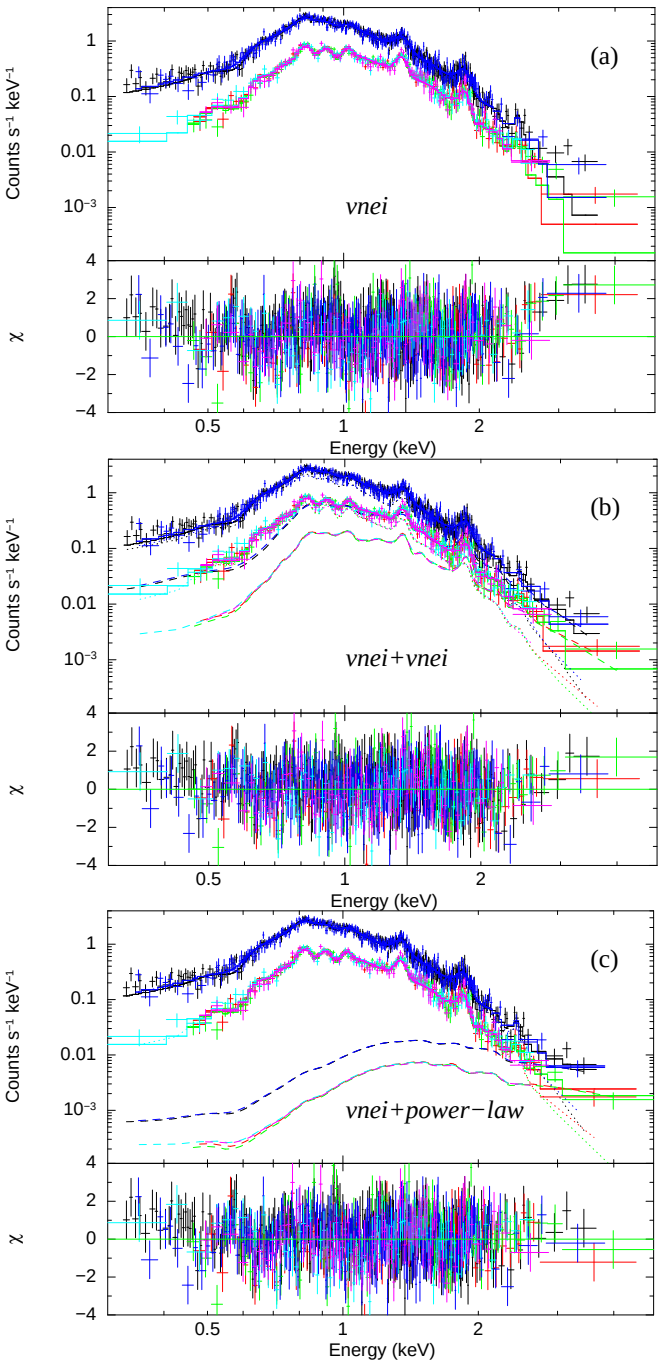

FIG. 4.— *XMM-Newton* EPIC spectra of the NE shell (region "Shell") fitted with absorbed *vnei* (a), *vnei+vnei* (b), and *vnei+powerlaw* (c) models. Each individual spectrum is adaptively binned to achieve a background-subtracted S/N of 3. Upper solid lines show pn spectra in black (observed in 2002) and blue (observed in 2003). Lower solid lines show MOS spectra colored in red, green (both observed in 2002), cyan and pink (both observed in 2003). The short and long dashed lines show the soft and hard components of the model, respectively.

XSPEC were initially applied to interpret the emission in the large NE region "Shell". We allow the abundances of C, Si, S, and Fe to vary, and tie the abundances of all other elements (N, O, Ne, Mg, Ar, Ca, and Ni) to that of C. The absorbed *vmekal* model does not produce a good fit to the soft X-ray spectra ($\chi^2_\nu \sim 1.75$), while the *vnei* model with a plasma temperature $kT = 0.33 \pm 0.1$ keV appears to provide a better fit ($\chi^2_\nu \sim 1.33$); however it seriously underestimates the flux above 2.5 keV as shown in Figure 4(a). We therefore added another component to account for the hard X-ray tail in the spectra; and the addition can be either a second NEI plasma model or a *powerlaw* one. The obtained χ^2_ν values are 1.22 and 1.28, respectively, corresponding to *F*-test null hypothesis probabilities of 1.1×10^{-17} and 3.6×10^{-10} for adding the hard components, which supports the need for a two-component model.

The spectra fitted with the absorbed single *vnei*, double *vnei*, and *vnei+powerlaw* models are shown in Figure 4 and the fitting results are tabulated in Table 2. The three models commonly support the origin of the soft X-ray emission being a ~ 0.3 keV plasma with under-solar abundances (except for [S/H]~ 1 in the *vnei+powerlaw* model). The double-*vnei* model reproduces the spectra well in the soft X-ray band (≤ 3 keV) and gives the best fit among the three models in view of χ^2_ν. The cold component has a temperature $kT_{\rm c} \sim 0.3$ keV (with ionization timescale τ_c poorly constrained), while the hot component has a temperature $kT_{\rm h} \sim 0.6$ keV and is underionized ($\tau_h \sim 1 \times 10^{12}\,{\rm cm^{-3}\,s}$). The *vnei+powerlaw* model also reproduces well the X-ray spectra of the NE shell. It is actually reasonable to search in the shell for non-thermal X-rays that are produced by the electrons accelerated at the shock sites, considering that the shell is spatially correlated with the γ-ray-emitting area that interacts with the MC. In this model, the X-ray emission from the shell consists of a thermal component characterized by a relatively cold ($kT = 0.3$ keV) plasma with ionization timescale $\tau_c > 7.6 \times 10^{11}$ cm^{-3} s and low metal abundances (except for S), plus a non-thermal component with a hard photon index ($\Gamma = 1.9^{+0.5}_{-1.0}$). Compared to the double-*vnei* model, the *vnei+powerlaw* model fits the hard X-ray band (3–5 keV) better[11] but has slightly larger residuals in the soft band. Note that there are only a few bins above 3 keV, which play a minor role in affecting the χ^2_ν value. The lack of sufficient counts above 3 keV does not allow us to distinguish between the two models. Deeper observations are needed, especially to improve on the statistics of the hard X-ray emission above ~ 3 keV.

We further examine the spectral properties of two separate regions, "S1" and "S2", along the shell, in light of the deformed morphology of the shell and the non-uniform environment at the NE boundary. We also applied the double-*vnei* and *vnei+powerlaw* models to fit the spectra and the fitting results are summarized in Table 2. The X-ray emission of the small-scale regions share similar spectral properties to those of the larger region "Shell" based on the available *XMM-Newton* data.

[11] We did not detect any source emission with S/N≥ 3 between 5 and 8 keV. The best-fit results of the *vnei+powerlaw* model gives a flux of $\sim 7 \times 10^{-14}$ erg cm^{-2} s^{-1} in the 5–8 keV range, which is, however, about an order of magnitude smaller than the background level. This explains the lack of background-subtracted spectral bins above 5 keV. We also simulated the spectra using the best-fit results of the *vnei+ powerlaw* model to check if we can obtain a few bins above 5 keV with the given response files and exposure time. Only two bins are obtained in the MOS spectra but they span from < 4 keV to 8 keV thus are not statistically important.

TABLE 2
SPECTRAL FITTING RESULTS FOR THE NORTHEASTERN SHELL OF W28 WITH 90% CONFIDENCE

Regions	Shell			S1		S2	
Models	*vnei*	*vnei+vnei*[a]	*vnei+powerlaw*	*vnei+vnei*[a]	*vnei+powerlaw*	*vnei+vnei*[a]	*vnei+powerlaw*
χ^2_ν (dof)	1.33 (1019)	1.23 (1016)	1.28 (1017)	1.12 (833)	1.14 (834)	1.17 (783)	1.19 (784)
$N_{\rm H}$ (10^{21} cm^{-2})	$7.87^{+0.23}_{-0.27}$	$7.76^{+0.31}_{-0.13}$	$8.15^{+0.25}_{-0.23}$	$7.93^{+0.37}_{-0.34}$	$8.19^{+0.33}_{-0.32}$	$7.50^{+0.48}_{-0.44}$	$7.63^{+0.35}_{-0.35}$
Soft component							
$kT_{\rm c}$ (keV)	$0.33^{+0.01}_{-0.01}$	$0.29^{+0.01}_{-0.01}$	$0.30^{+0.01}_{-0.01}$	$0.29^{+0.01}_{-0.01}$	$0.30^{+0.02}_{-0.01}$	$0.29^{+0.02}_{-0.01}$	$0.31^{+0.02}_{-0.01}$
$\tau_{\rm c}$ (10^{12} cm^{-3} s)	$0.60^{+0.15}_{-0.20}$	< 500	1.06 (> 0.76)	< 500	1.14(> 0.56)	< 500	1.10(> 0.74)
Abun[b]	$0.26^{+0.03}_{-0.03}$	$0.44^{+0.10}_{-0.09}$	$0.33^{+0.11}_{-0.06}$	$0.47^{+0.17}_{-0.11}$	$0.34^{+0.16}_{-0.07}$	$0.34^{+0.10}_{-0.09}$	$0.27^{+0.08}_{-0.05}$
[Si/H]	$0.40^{+0.08}_{-0.07}$	$0.43^{+0.08}_{-0.07}$	$0.59^{+0.18}_{-0.10}$	$0.50^{+0.11}_{-0.08}$	$0.61^{+0.07}_{-0.14}$	$0.34^{+0.09}_{-0.09}$	$0.43^{+0.14}_{-0.10}$
[S/H]	$0.88^{+0.30}_{-0.27}$	$0.37^{+0.20}_{-0.17}$	$1.04^{+0.30}_{-0.38}$	$0.46^{+0.28}_{-0.24}$	$1.11^{+0.43}_{-0.46}$	$0.44^{+0.27}_{-0.24}$	$1.04^{+0.42}_{-0.43}$
[Fe/H]	$0.22^{+0.03}_{-0.03}$	$0.41^{+0.07}_{-0.07}$	$0.29^{+0.02}_{-0.05}$	$0.45^{+0.15}_{-0.11}$	$0.30^{+0.17}_{-0.07}$	$0.34^{+0.08}_{-0.08}$	$0.23^{+0.05}_{-0.06}$
$F_{\rm s}$ (10^{-11} erg cm^{-2} s^{-1})[c]	6.61	4.98	7.72	2.72	3.86	1.89	2.52
Hard component							
$kT_{\rm h}$ (keV)	···	$0.61^{+0.07}_{-0.06}$	···	$0.63^{+0.06}_{-0.06}$	···	$0.65^{+0.34}_{-0.08}$	···
$\tau_{\rm h}$ (10^{12} cm^{-3} s)	···	$0.79^{+0.85}_{-0.33}$	···	0.80 (> 0.35)	···	$0.44^{+0.55}_{-0.32}$	···
Γ	···	···	$1.85^{+0.54}_{-0.98}$	···	$0.24^{+1.87}_{-2.25}$	···	$1.32^{+1.04}_{-1.81}$
$F_{\rm h}$ (10^{-12} erg cm^{-2} s^{-1})[c]	···	7.59	0.34	3.01	0.11	2.20	0.09

NOTE. — Three models are applied to fit the spectra of the NE region "Shell". Two-component models better reproduce the hard X-ray emission and are thus subsequently used for the small-scale regions "S1" and "S2". The parameters for the hard components show the fit results of the two-component models, where the temperature $kT_{\rm h}$ and ionization timescale $\tau_{\rm h}$ are only applied for the hot component in the *vnei+vnei* model, while Γ is the photon index of *powerlaw* component. See the spectra of region "Shell" in Figure 4.

[a] The abundances of the soft and hard component are coupled.
[b] The tied abundances of C, N, O, Ne, Mg, Ar, Ca, and Ni.
[c] The best-fitted unabsorbed fluxes $F_{\rm s}$ (soft component) and $F_{\rm h}$ (hard component) in the 0.3–5.0 keV range.

3.3.3. *Central Gas*

We first focus on the larger central region "C" which encircles the brightest X-ray-emitting gas in the SNR interior. This region has a similar sky coverage with the "center" region defined in RB02. There are three distinct line features, Mg Heα, Si Heα, and S Heα, and several weaker bumps contributed from Kα lines such as H-like Mg ($\sim$ 1.47 keV) and Si ($\sim$ 2.0 keV), confirming the thermal origin of the X-ray emission. We ignore the bins above 5 keV in the following spectral fitting of the central X-ray because of the poor statistics and the spectrum being background dominated. Although an excess is seen above 5 keV in both pn and MOS spectra, we do not discuss its nature in this paper given that the strength of this excess is not statistically significant.

Single-temperature CIE (*vmekal*) and NEI (*vnei*) models were first applied to the central region. We allow the abundances of C, Mg, Si, S and Fe to vary, and tied the abundances of all other elements to C. The fit results are summarized in the second and third columns of Table 3. The *vmekal* and *vnei* models give a similar foreground hydrogen column density ($N_{\rm H} \sim 4 \times 10^{21}$ cm^{-2}) and plasma temperature ($kT \sim 0.6$ keV), which also agreeably support low elemental abundances of the hot plasma. However, we find that none of the *vmekal* and *vnei* models yield adequately good fits to the spectra ($\chi^2_\nu \sim 1.6$ and ~ 1.7, respectively) since they failed to account for the emission above 2.5 keV and for the weak bump at around 2.0 keV probably due to the Lyα line of Si.

To better reproduce the spectra, a two-component model *vnei+vnei* was subsequently fitted, with the abundances of the cold and hot components tied together. The two-temperature NEI model improved the fitting to some extent ($\chi^2_\nu \sim 1.4$) and gave a low ionization timescale ($\tau_{\rm c} \sim 2 \times 10^{11}$ cm^{-3} s) for the cold component. Whereas, a much higher ionization timescale ($\tau_{\rm h} \sim 10^{12}$ cm^{-3} s with the upper limit being unconstrained) is obtained for the hot component, implying the hotter gas is (or close to) in ionization equilibrium.

We accordingly use a *vmekal* model instead of *vnei* to describe the hot component. The *vnei+vmekal* model gives a satisfactory fit ($\chi^2_\nu \sim 1.3$, see Table 4 and the upper-left panel of Figure 5). The spectral fit results show that, on average, the X-ray-emitting gas in the SNR interior has a low metal abundance (below solar values) and is composed of a cold ($kT_{\rm c} \sim 0.4$ keV) and underionized ($\tau_{\rm c} \sim 4 \times 10^{11}$ cm^{-3} s) plasma and a hot ($kT_{\rm h} \sim 0.8$ keV) plasma in CIE.

Given that the gas in the SNR interior is not uniform in either X-rays or the other bands (see Figure 1(b)) and region "C" is large in scale (14′), we subsequently extracted five smaller regions ("CN", "C1", "C2", "C3" and "C4") to inspect any spatial variation of the gas properties in the central portion. In Table 4 we summarize the *vnei+vmekal* fit results of the five small-scale regions, and in Figure 5 we show the EPIC spectra with the fitted models. As shown in the table, the absorption column density is generally increased from west to east, while the temperature is generally decreased. The highest absorption ($N_{\rm H} \sim 7 \times 10^{21}$ cm^{-2}) and lowest temperature ($kT_{\rm c} \sim 0.3$ keV) are found in the northern region "CN", which is on the inner shell and bright in CO and Hα emission (see Figure 1(b)).

We also examined whether a recombining plasma model could fit the *XMM-Newton* spectra in the six central regions, considering that there is a weak bump at around 2.0 keV for the H-like Si line and that SK12 had adopted a recombining scenario to explain the plasma in the SNR interior. We applied the NEI jump (*neij*) model in SPEX, which describes a CIE plasma with initial temperature T_i rapidly heated/cooled to a tempera-

TABLE 3
SPECTRAL FITTING RESULTS FOR THE CENTRAL GAS OF W28 WITH SINGLE-COMPONENT MODELS

Models	*vmekal*	*vnei*	*neij*					
Regions	C	C	C	CN	C4	C3	C2	C1
χ^2_ν (d.o.f.)	1.59 (622)	1.69 (621)	1.44 (620)	1.44 (454)	1.07 (539)	1.35 (438)	1.18 (496)	1.17 (392)
$N_{\rm H}$ (10^{21} cm^{-2})	$4.05^{+0.09}_{-0.09}$	$4.37^{+0.17}_{-0.10}$	$3.98^{+0.10}_{-0.09}$	$3.84^{+0.21}_{-0.06}$	$3.87^{+0.24}_{-0.08}$	$3.69^{+0.22}_{-0.20}$	$4.11^{+0.20}_{-0.18}$	$4.25^{+0.32}_{-0.09}$
kT (keV)	$0.60^{+0.01}_{-0.01}$	$0.60^{+0.01}_{-0.01}$	$0.59^{+0.01}_{-0.01}$	$0.59^{+0.01}_{-0.02}$	$0.57^{+0.02}_{-0.02}$	$0.54^{+0.01}_{-0.03}$	$0.59^{+0.02}_{-0.01}$	$0.63^{+0.04}_{-0.02}$
τ[a] (10^{11} cm^{-3} s)	···	$2.35^{+0.21}_{-0.24}$	$8.58^{+0.61}_{-0.86}$	$13.54^{+2.50}_{-3.19}$	$8.20^{+0.40}_{-1.34}$	$8.66^{+0.63}_{-2.43}$	$8.36^{+0.41}_{-1.22}$	$7.45^{+3.59}_{-1.53}$
Abun[b]	$0.18^{+0.02}_{-0.02}$	$0.12^{+0.01}_{-0.01}$	$0.22^{+0.02}_{-0.02}$	$0.31^{+0.02}_{-0.06}$	$0.22^{+0.03}_{-0.05}$	$0.13^{+0.02}_{-0.03}$	$0.33^{+0.08}_{-0.06}$	$0.29^{+0.03}_{-0.11}$
[Mg/H]	$0.26^{+0.03}_{-0.02}$	$0.12^{+0.01}_{-0.01}$	$0.37^{+0.02}_{-0.04}$	$0.60^{+0.05}_{-0.12}$	$0.53^{+0.13}_{-0.09}$	$0.28^{+0.08}_{-0.04}$	$0.46^{+0.05}_{-0.08}$	$0.44^{+0.05}_{-0.10}$
[Si/H]	$0.18^{+0.02}_{-0.02}$	$0.16^{+0.02}_{-0.02}$	$0.25^{+0.03}_{-0.02}$	$0.29^{+0.04}_{-0.05}$	$0.33^{+0.04}_{-0.05}$	$0.25^{+0.04}_{-0.04}$	$0.34^{+0.04}_{-0.06}$	$0.25^{+0.10}_{-0.05}$
[S/H]	$0.31^{+0.06}_{-0.06}$	$0.39^{+0.07}_{-0.07}$	$0.32^{+0.07}_{-0.07}$	$0.32^{+0.15}_{-0.15}$	$0.51^{+0.15}_{-0.15}$	$0.47^{+0.13}_{-0.13}$	$0.52^{+0.15}_{-0.14}$	$0.36^{+0.19}_{-0.18}$
[Fe/H]	$0.12^{+0.01}_{-0.01}$	$0.10^{+0.01}_{-0.01}$	$0.18^{+0.01}_{-0.01}$	$0.21^{+0.02}_{-0.02}$	$0.21^{+0.01}_{-0.04}$	$0.14^{+0.01}_{-0.02}$	$0.26^{+0.03}_{-0.04}$	$0.26^{+0.04}_{-0.05}$
$fn_e n_{\rm H} V d_2^{-2}$ (10^{57} cm^{-3})	$6.29^{+0.32}_{-0.31}$	$7.45^{+0.35}_{-0.46}$	$5.91^{+0.38}_{-0.36}$	$0.92^{+0.14}_{-0.12}$	$0.78^{+0.13}_{-0.11}$	$1.21^{+0.23}_{-0.17}$	$1.20^{+0.17}_{-0.15}$	$0.88^{+0.16}_{-0.13}$
$n_{\rm H} f^{1/2} d_2^{1/2}$ (cm^{-3})[c]	$0.79^{+0.02}_{-0.02}$	$0.86^{+0.02}_{-0.03}$	$0.77^{+0.02}_{-0.02}$	$0.67^{+0.05}_{-0.04}$	$0.88^{+0.07}_{-0.06}$	$1.07^{+0.10}_{-0.07}$	$0.93^{+0.07}_{-0.06}$	$0.87^{+0.08}_{-0.06}$
F (10^{-11} erg cm^{-2} s^{-1})[d]	8.99	10.43	8.72	1.63	1.23	1.49	2.17	1.50
kT_i (keV)[e]	···	···	> 6.49	> 1.34	> 2.20	> 1.91	> 2.68	> 5.17
Average charge								
Mg	···	···	$11.11^{+0.06}_{-0.06}$	$10.90^{+0.14}_{-0.12}$	$11.09^{+0.12}_{-0.09}$	$11.01^{+0.19}_{-0.14}$	$11.10^{+0.11}_{-0.05}$	$11.23^{+0.16}_{-0.20}$
Si	···	···	$12.65^{+0.09}_{-0.07}$	$12.35^{+0.18}_{-0.16}$	$12.66^{+0.20}_{-0.14}$	$12.58^{+0.26}_{-0.18}$	$12.66^{+0.14}_{-0.09}$	$12.80^{+0.21}_{-0.31}$
S	···	···	$14.34^{+0.08}_{-0.06}$	$14.09^{+0.14}_{-0.12}$	$14.35^{+0.16}_{-0.18}$	$14.28^{+0.26}_{-0.21}$	$14.35^{+0.14}_{-0.13}$	$14.48^{+0.22}_{-0.09}$
Fe	···	···	$18.08^{+0.36}_{-0.44}$	$17.39^{+0.37}_{-0.20}$	$17.98^{+0.81}_{-0.83}$	$17.55^{+1.17}_{-0.80}$	$18.07^{+0.68}_{-0.67}$	$18.85^{+1.27}_{-1.23}$
kT_z (keV)								
Mg	···	···	$0.72^{+0.02}_{-0.02}$	$0.65^{+0.05}_{-0.04}$	$0.71^{+0.03}_{-0.03}$	$0.69^{+0.07}_{-0.05}$	$0.72^{+0.04}_{-0.02}$	$0.77^{+0.08}_{-0.08}$
Si	···	···	$0.91^{+0.05}_{-0.03}$	$0.75^{+0.10}_{-0.10}$	$0.92^{+0.10}_{-0.07}$	$0.88^{+0.13}_{-0.10}$	$0.92^{+0.07}_{-0.05}$	$0.99^{+0.12}_{-0.16}$
S	···	···	$1.12^{+0.08}_{-0.05}$	$0.85^{+0.17}_{-0.22}$	$1.13^{+0.14}_{-0.18}$	$1.07^{+0.23}_{-0.25}$	$1.13^{+0.13}_{-0.12}$	$1.24^{+0.19}_{-0.27}$
Fe	···	···	$0.69^{+0.04}_{-0.05}$	$0.61^{+0.04}_{-0.02}$	$0.68^{+0.09}_{-0.10}$	$0.63^{+0.13}_{-0.10}$	$0.69^{+0.07}_{-0.08}$	$0.78^{+0.16}_{-0.14}$

NOTE. — The second and third columns show the fitting results of the absorbed *vmekal* and *vnei* models in XSPEC, respectively, (*vnei*+*vmekal* model is shown in Table 4), for region "C". In the last six columns, an absorbed recombining plasma model *neij* in SPEX is applied for region "C" and 5 smaller regions (see spectra in Figure 6). Statistical errors of the fitted parameters are given at the 90% confidence level, except the error ranges of the average charge and kT_z, which are instead estimated using the 90% confidence ranges of kT, kT_i, and τ.

[a] τ represents the ionization timescale for the *vnei* model, while it is the recombination timescale for the *neij* model.
[b] The tied abundances of C, N, O, Ne, Ar, Ca, and Ni.
[c] For the density estimates, we assume a sphere for region "C" and short cylinders for all other rectangle regions.
[d] The unabsorbed fluxes in the 0.3–5.0 keV band.
[e] The best-fit values of the initial electron temperatures all reach the upper limit of 10 keV and the error bars are poorly constrained.

ture T, observed after relaxation with a timescale t. The fit results of the *neij* model are tabulated in Table 3 and the spectra are shown in Figure 6. In this recombining plasma model, the electrons of the X-ray-emitting plasma in the region "C" with initial temperature $kT_i > 6.5$ keV rapidly cool to a temperature of 0.6 keV after a timescale t (the recombination time scale $n_{\rm e}t \simeq 8.6\times10^{11}$ cm^{-3} s). The foreground column density (4.0×10^{21} cm^{-2}) and electron temperature (0.6 keV) is similar to those from the single *vmekal* and *vnei* models, while the average charges of Mg, Si, S, and Fe (11.11, 12.65, 14.34, and 18.08, respectively) are larger than those expected from a 0.6-keV CIE plasma (10.71, 12.11, 13.95, and 17.22, respectively). The estimated ionization temperatures of the four elements (0.7, 0.9, 1.1, and 0.7 keV, respectively) are all higher than the electron temperature, indicating the four elements are over-ionized. The most prominent residuals are shown as a bump at around 1.34 keV. Adding a Gaussian line to compensate for the residuals, we found that the bump is centered at $1.34^{+0.01}_{-0.02}$ keV and has a width of $0.21^{+0.02}_{-0.04}$ keV ($\chi^2_\nu = 1.24$). Some of the residuals at $\sim$ 1.17–1.29 keV may result from the incomplete atomic data for Fe L-shell transition of SPEX code ($n = 6, 7, 8 \rightarrow 2$ for Fe XVII, $n = 6, 7 \rightarrow 2$ for Fe XVIII, and $n = 6 \rightarrow 2$ for Fe XIX; Brickhouse et al. 2000; Audard et al. 2001; also pointed out by SK12). However, most residuals are above 1.3 keV and may result from the fit itself rather than the incompleteness of the atomic data.

We further applied the recombining plasma model *neij* to the five smaller regions. As shown in Table 3, the model gives a smaller variation of temperature (0.54–0.63 keV) and column density (3.7–4.3×10^{21} cm^{-2}) than given by a *vnei*+*vmekal* model. Compared to the two-temperature model, the recombining plasma model gives similar χ^2_ν value for region "C2" and a marginally poorer fit for regions "C1" and "C4". Hence, we cannot exclude either of the two-temperature or the recombining plasma model for the three smaller scale regions with the current available *XMM-Newton* observations. However, for regions "CN" and "C3", the χ^2_ν values of the *neij* spectral fits are apparently larger than those of the two-temperature model (1.44 and 1.35 versus 1.26 and 0.98, respectively). We added a Gaussian line for regions "CN" and "C3" to compensate for the residuals at around 1.3 keV and found that the fits ($\chi^2_\nu = 1.36$ and 1.28, respectively) are still poorer than the two-temperature model, which implies that the latter model provides a better fit to the data for the two regions.

TABLE 4
Spectral fitting results for the central gas of W28 with a two-component model

Regions	C	CN	C4	C3	C2	C1
χ^2_ν (d.o.f.)	1.32 (619)	1.26 (453)	1.04 (549)	0.98 (437)	1.18 (495)	1.12 (391)
$N_{\rm H}$ (10^{21} cm^{-2})	$5.50^{+0.45}_{-0.56}$	$7.24^{+0.96}_{-1.01}$	$5.91^{+0.84}_{-1.00}$	$3.86^{+0.35}_{-0.30}$	$4.33^{+1.32}_{-0.20}$	$3.57^{+0.50}_{-0.41}$
Cold component						
$kT_{\rm c}$ (keV)	$0.36^{+0.06}_{-0.04}$	$0.28^{+0.05}_{-0.03}$	$0.31^{+0.07}_{-0.05}$	$0.57^{+0.02}_{-0.05}$	$0.54^{+0.04}_{-0.04}$	$0.64^{+0.03}_{-0.03}$
$\tau_{\rm c}$ (10^{11} cm^{-3} s)	$4.34^{+2.93}_{-1.73}$	$5.14^{+12.04}_{-2.97}$	5.03(> 1.72)	< 500	$1.54^{+0.60}_{-0.70}$	7.28(> 1.48)
Abun[a]	$0.17^{+0.02}_{-0.03}$	$0.30^{+0.11}_{-0.09}$	$0.14^{+0.06}_{-0.05}$	$0.31^{+0.17}_{-0.15}$	$0.15^{+0.06}_{-0.05}$	$0.49^{+0.40}_{-0.32}$
[Mg/H]	$0.30^{+0.04}_{-0.03}$	$0.75^{+0.21}_{-0.18}$	$0.44^{+0.10}_{-0.09}$	$0.44^{+0.21}_{-0.15}$	$0.37^{+0.08}_{-0.08}$	$0.71^{+0.43}_{-0.45}$
[Si/H]	$0.24^{+0.03}_{-0.04}$	$0.45^{+0.16}_{-0.12}$	$0.34^{+0.09}_{-0.08}$	$0.37^{+0.15}_{-0.12}$	$0.34^{+0.08}_{-0.08}$	$0.44^{+0.25}_{-0.22}$
[S/H]	$0.34^{+0.06}_{-0.07}$	$0.39^{+0.23}_{-0.19}$	$0.53^{+0.22}_{-0.18}$	$0.52^{+0.23}_{-0.21}$	$0.42^{+0.14}_{-0.14}$	$0.32^{+0.29}_{-0.24}$
[Fe/H]	$0.19^{+0.03}_{-0.02}$	$0.44^{+0.11}_{-0.13}$	$0.27^{+0.06}_{-0.07}$	$0.25^{+0.05}_{-0.06}$	$0.31^{+0.05}_{-0.05}$	$0.40^{+0.18}_{-0.16}$
$f_{\rm c} n_{e,c} n_{{\rm H},c} V d_2^{-2}$ (10^{57} cm^{-3})	$7.78^{+2.86}_{-2.61}$	$3.15^{+2.69}_{-1.55}$	$1.61^{+1.68}_{-0.79}$	$0.56^{+0.21}_{-0.15}$	$0.67^{+0.20}_{-0.12}$	$0.30^{+0.22}_{-0.10}$
$n_{{\rm H},c} d_2^{1/2}$ (cm^{-3})[b]	1.48	1.79	2.03	1.04	1.17	0.91
$F_{\rm c}$ (10^{-11} erg cm^{-2} s^{-1})[c]	10.36	6.02	2.06	1.13	1.58	0.84
Hot component						
$kT_{\rm h}$ (keV)	$0.77^{+0.02}_{-0.02}$	$0.78^{+0.06}_{-0.04}$	$0.78^{+0.04}_{-0.04}$	$1.20^{+0.21}_{-0.25}$	$1.00^{+0.06}_{-0.06}$	$1.40^{+0.19}_{-0.35}$
$f_{\rm h} n_{e,h} n_{{\rm H},h} V d_2^{-2}$ (10^{57} cm^{-3})	$3.09^{+0.26}_{-0.23}$	$0.44^{+0.11}_{-0.09}$	$0.40^{+0.07}_{-0.07}$	$0.13^{+0.10}_{-0.04}$	$0.36^{+0.08}_{-0.06}$	$0.14^{+0.08}_{-0.03}$
$f_{\rm h}^{\rm d}$	0.65	0.52	0.61	0.52	0.65	0.69
$n_{{\rm H},h} d_2^{1/2}$ (cm^{-3})[b]	0.69	0.64	0.81	0.50	0.63	0.42
$F_{\rm h}$ (10^{-11} erg cm^{-2} s^{-1})[c]	5.52	1.24	0.83	0.28	0.75	0.32

Note. — An absorbed thermal model *vnei* (cold component)+*vmekal* (hot component) is used for region "C" and 5 smaller regions (see spectra in Figure 5). The metal abundances of the cold and hot components are coupled. Statistical errors are given at the 90% confidence level.

[a] The tied abundances of C, N, O, Ne, Ar, Ca, and Ni.

[b] In the estimate of densities, we assume a sphere for region "C" and short cylinders for all other rectangular regions.

[c] The unabsorbed fluxes of the cold component ($F_{\rm c}$) and of the hot component ($F_{\rm h}$) are in the 0.3–5.0 keV band.

[d] Volume filling factor of the hot-phase gas $f_{\rm h} = 1 - f_{\rm c}$, where the filling factor of the cold-phase gas $f_{\rm c} = (1 + (T_{\rm h}/T_{\rm c})^2 ({\rm norm_h}/{\rm norm_c}))^{-1}$.

4. DISCUSSION

4.1. *Global Gas Properties*

We have performed an *XMM-Newton* imaging and spatially-resolved spectroscopic study of the MM SNR W28. In the X-ray band, the remnant shows a centrally peaked morphology and blobby structures in the SNR interior. The limb-brightened shell in the northeast appears distorted by the impact with dense ambient medium.

4.1.1. *Gas Properties of the NE Shell*

The X-ray emission from the NE limb is best described by a combination of a $kT = 0.3$ keV thermal component with sub-solar metal abundances and a hard component of either thermal or non-thermal origin (see Section 3.3.2 for details). We investigated the possible spatial variation of the gas properties by dividing the bright NE shell into two smaller regions "S1" and "S2". No apparent variations have been found between them.

According to the *vnei+powerlaw* model, the density of the X-ray-emitting gas in region "Shell" can be estimated from the volume emission measure $f n_e n_{\rm H} V = 4.4 \pm 0.6 \times 10^{57} d_2^2$ cm^{-3}, where f is the filling factor of the X-ray-emitting plasma within the volume V, n_e and $n_{\rm H}$ are the electron and hydrogen density of the gas, respectively, and $d_2 = d/2$ kpc is the distance scaled with 2 kpc. Assuming an oblate spheroid for the elliptical region "Shell" (with half-axes $3\farcm68 \times 3\farcm68 \times 1\farcm56$) and $n_e = 1.2 n_{\rm H}$, the mean hydrogen density and the mass of the X-ray emitting gas are obtained to be $n_{\rm H} = 2.7 \pm 0.2 f^{-1/2} d_2^{-1/2}$ cm^{-3} and $M_{\rm X} = 1.6 \pm 0.1 f^{1/2} d_2^{5/2}$ $M_\odot$, respectively. The ambient density is thus estimated to be $n_0 = n_{\rm H}/4 \sim 0.7 f^{-1/2} d_2^{-1/2}$ cm^{-3}. The ionization age inferred from the ionization timescale $n_e t_i$ is $t_{\rm i} > 7.5 f^{1/2} d_2^{1/2}$ kyr.

The two-temperature (0.3 keV+0.6 keV) model can also represent the spectra of the NE shell. We assume that the two-phase gas fills the whole volume (with filling factors $f_{\rm c} + f_{\rm h} = 1$) and is in pressure equilibrium. The colder gas is found to fill 68% of the volume, with a density $n_{{\rm H},c} = 2.5 \pm 0.3 (f_{\rm c}/0.68)^{-1/2} d_2^{-1/2}$ cm^{-3}, while the hotter gas has a density $n_{{\rm H},h} = 1.2 \pm 0.2 (f_{\rm h}/0.32)^{-1/2} d_2^{-1/2}$ cm^{-3}. The mass of the cold and hot components is estimated to be $\sim 1.0 (f_{\rm c}/0.68)^{1/2} d_2^{5/2}$ $M_\odot$ and $\sim 0.2 (f_{\rm h}/0.32)^{1/2} d_2^{5/2}$ $M_\odot$, respectively. As the X-ray emission is emitted from the shock–cloud interaction region, the hot plasma may consist of two density components: (1) the dense cloud material and (2) the tenuous inter-cloud medium. The denser cloud material heated by the transmitted shock is relatively colder, which is responsible for the 0.3 keV component, while the inter-cloud medium may give arise to the $\sim$ 0.6 keV component, as also seen in the shells of the Vela SNR (Bocchino et al. 1999; Miceli et al. 2006) and the Cygnus Loop (Zhou et al. 2010). The ionization timescale (0.5–1.6×10^{12} cm^{-3} s) of the hot inter-cloud gas can provide a rough estimation of its ionization age of 1–4×10^4 yr. Therefore, both of the two-temperature and *vnei+powerlaw* models suggest an evolved stage for

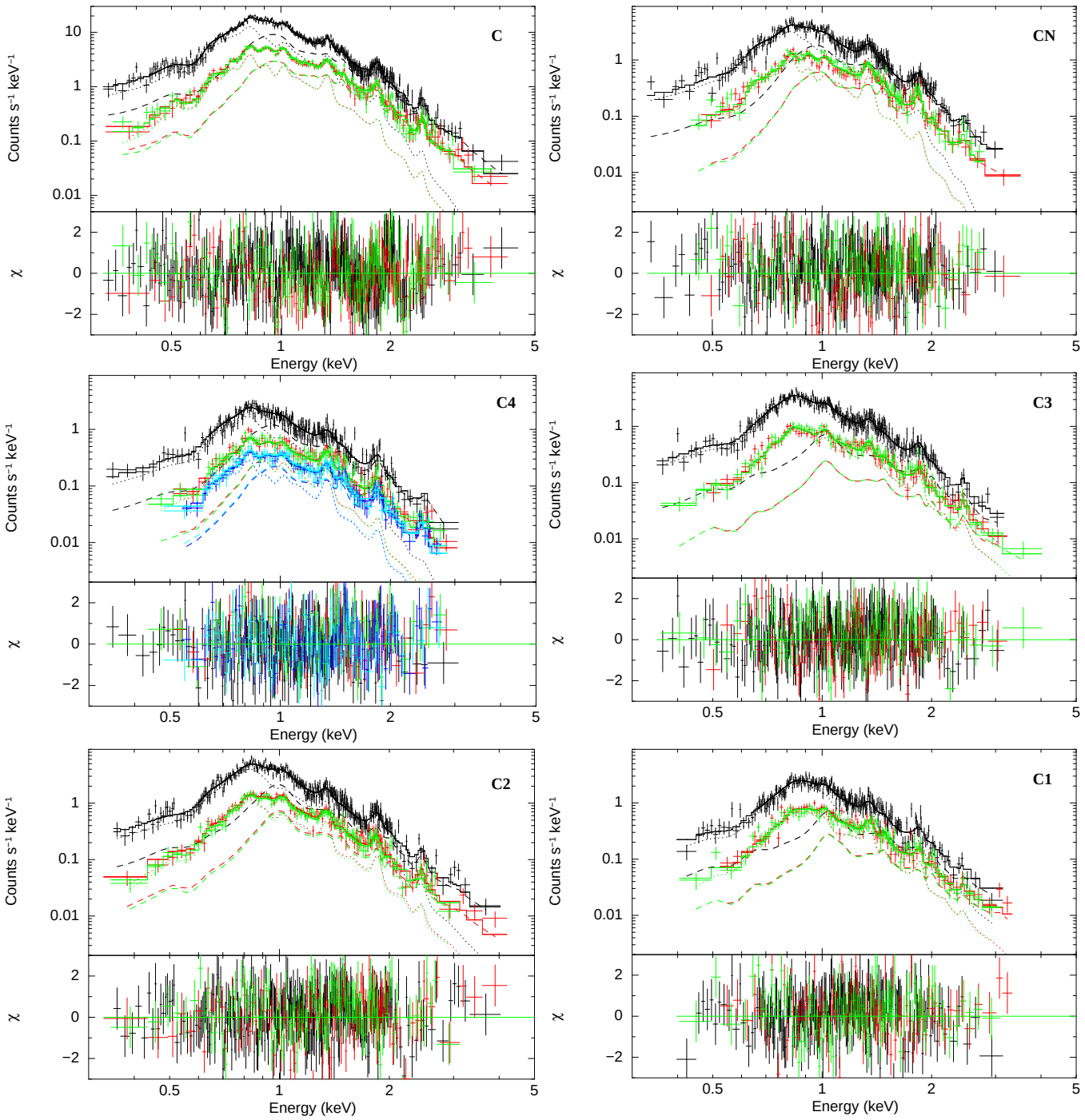

FIG. 5.— *XMM-Newton* EPIC spectra and fitted model (absorbed *vnei+vmekal*) from the six regions (indicated in Figure 2) in the SNR interior. Each individual spectrum is adaptively binned to achieve a background-subtracted S/N of 3. The black solid lines show pn spectra, while MOS spectra are shown by the lower solid lines in red and green. The blue and cyan lines for region "C4" represent MOS1 spectra extracted from the southwestern edge of the NE observations with IDs 0145970101 and 0145970401, respectively. The short and long dashed lines show the soft and hard components of the model, respectively.

W28.

4.1.2. *Recombining Plasma in the Interior of W28?*

We found that a recombining plasma model for over-ionized gas could fit the spectra of the central region, although the model is neither the only plausible one nor the best-fit one when compared with the two-temperature model (see Section 3.3.3). In this model, the central X-rays arise from a recombining plasma with an electron temperature $kT = 0.59$ keV, and multiple ionization temperatures of elements increasing from Mg ($kT_z = 0.72$ keV) to S ($kT_z = 1.12$ keV) and dropping at Fe ($kT_z = 0.69$ keV). Another multi-kT_z model is previously used by SK12, although different kT_z and kT values were obtained (see further discussion in Section 4.2). The monotonic rise of the ionization temperature with atomic number except for Fe was explained by the element-dependent recombination timescale (SK12;

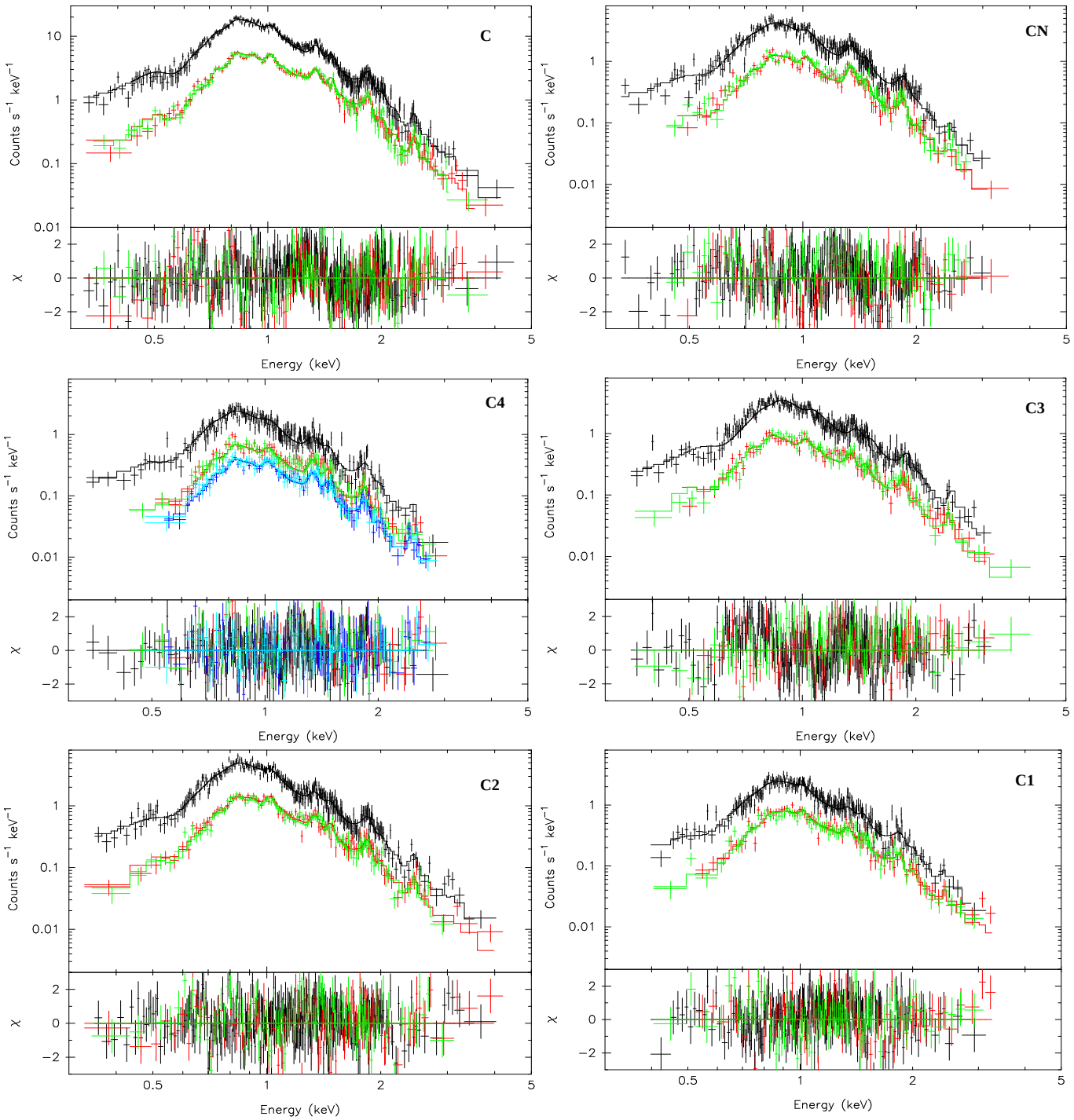

FIG. 6.— *XMM-Newton* EPIC spectra and fitted recombining plasma model from the six regions (indicated in Figure 2) in the SNR interior. Each individual spectrum is adaptively binned to achieve a background-subtracted S/N of 3. The black solid lines show pn spectra, while MOS spectra are shown by the lower solid lines in red and green. The blue and cyan lines for region "C4" represent MOS1 spectra extracted from the southwestern edge of the NE observations with observation IDs 0145970101 and 0145970401, respectively.

Smith & Hughes 2010). Assuming the filling factor of the X-ray-emitting gas is close to 1, the hydrogen density of the gas is estimated as $n_{\rm H} \sim 0.8 d_2^{-1/2}$ cm^{-3}. The recombination age is inferred from the recombination timescale $t_{\rm rec} = \tau/n_e \sim 2.9 \times 10^4 d_2^{1/2}$ yr, slightly lower than but consistent with the dynamical age of W28 (3–4×10^4 yr).

By applying the recombining plasma model to the five smaller regions, we found a small spatial variation of the parameters. The electron temperature reaches a maximum in the western region "C1" ($\sim$ 0.63 keV) and a minimum at region "C3" ($\sim$ 0.54 keV). The recombination ages of regions "C1", "C2", "C3", and "C4" are estimated as 2.3×10^4 yr, 2.4×10^4 yr, 2.1×10^4 yr, and 2.5×10^4 yr, respectively, while the region "CN", which is basically along the inner radio shell, shows the longest recombination age ($\sim 5.3 \times 10^4$ yr) with the lowest metal

TABLE 5
COMPARING OUR *XMM-Newton* SPECTRAL RESULTS FOR THE CENTRAL GAS WITH PREVIOUS X-RAY STUDIES

Telescope	*XMM-Newton*		*ASCA*/*ROSAT*	*ASCA*	*Suzaku*
Paper	Present		RB02	KO05[a]	SK12
Model	*vnei*+*vmekal*	*neij*	*vnei*+*vnei*	*vnei*+*vnei*	Multi-T_z Recombining
χ^2_ν (dof)	1.32 (619)	1.44 (620)	1.1 ($\sim$ 650)	1.06 (129)	1.41 (634)
$N_{\rm H}$ (10^{21} cm^{-2})	$5.5^{+0.4}_{-0.6}$	4.0 ± 0.1	6.6 ± 0.6	$5.1^{+0.8}_{-0.2}$	$4.7^{+0.2}_{-0.1}$
$kT_{\rm c}$ (keV)	$0.36^{+0.06}_{-0.04}$	0.59 ± 0.01	0.59 ± 0.05	0.62 ± 0.03	$0.40^{+0.02}_{-0.03}$
$\tau_{\rm c}^{\rm b}$ (10^{12} cm^{-3} s)	$0.43^{+0.29}_{-0.17}$	$0.86^{+0.06}_{-0.09}$	2($>$ 1)	31($>$ 2.7)	0.40($>$ 0.32)[c]
$kT_{\rm h}$ (keV)	$0.77^{+0.02}_{-0.02}$	...	$1.8^{+0.7}_{-0.5}$	$1.41^{+0.26}_{-0.10}$	...
$\tau_{\rm h}$ (10^{12} cm^{-3} s)	...	...	$0.5^{+0.5}_{-0.4}$	$0.5^{+1.6}_{-0.2}$	...

NOTE. — Different source region (except current study and RB02 used similar source region "C") and background region are selected for spectral extractions in each study.
[a] The best-fit parameters for the central region indicated by the black rectangle shown in Figure 2.
[b] $\tau_{\rm c}$ represents the ionization timescale for the cold *vnei* component, while it is the recombination timescale for the multi-T_z model.
[c] See SK12 for the detailed calculation of the recombination timescale.

ionization temperatures (that are close to the electron temperature $kT \sim 0.6$ keV).

4.1.3. *Two-temperature Gas in the SNR Center*

The X-ray spectra of the gas in the central regions are best represented by a two-temperature model including an under-ionized cold phase and a CIE hot phase (see Table 4). We have not found any evidence of ejecta inside the SNR because all metal abundances are below the solar value. Under the assumption that the cold gas and hot gas in region "C" are in pressure equilibrium ($n_{{\rm H},c}T_{\rm c} = n_{{\rm H},h}T_{\rm h}$) and fill all the volume ($f_{\rm c} + f_{\rm h} = 1$), we obtain the filling factor of the two components as $f_{\rm c} \sim 0.35$ and $f_{\rm h} \sim 0.65$, with corresponding mean hydrogen densities $n_{{\rm H},c} \sim 1.5 d_2^{-1/2}$ cm^{-3} and $n_{{\rm H},h} \sim 0.7 d_2^{-1/2}$ cm^{-3}. The ionization age of the cold-phase gas is inferred to be around 7.7 kyr, shorter than the dynamical age of the SNR, implying the gas could be more recently shocked or evaporated. We also estimate the gas densities of the smaller, rectangular regions in the SNR interior by assuming short cylinders as the three-dimensional shapes. The derived parameters, including the densities, filling factors, unabsorbed fluxes of the two-phase gas in the five regions, are tabulated in Table 4.

The spatially resolved spectroscopic analysis allows us to find the variations of the physical properties. There is a large-scale column density gradient that decreases from the northeast to the southwest. The heaviest absorption occurs on the NE shell ("Shell": $N_{\rm H} \sim 8 \times 10^{21}$ cm^{-2}) and the inner shell ("CN": $N_{\rm H} \sim 7 \times 10^{21}$ cm^{-2}), while the lowest one is found in the west of the remnant ("C1": $N_{\rm H} \sim 4 \times 10^{21}$ cm^{-2}). The large-scale absorption distribution is consistent with the optical reddening dropping from the northeast to the X-ray center (Long et al. 1991), which both agree with the picture that considerable molecular gas is located in the northeast. The enhanced absorption on the inner radio shell also favors that the inner shell is a shock–MC interaction interface projected to the northern hemisphere (Dubner et al. 2000).

We also found a temperature variation inside W28, which generally shows an opposite trend against the absorption. The temperature of the cold component drops by a factor two from the western region ("C1") to the inner radio shell ("CN") and in the east ("C4"); in the latter regions, the gas density of the cold component is higher than that in the west. Such variations of the foreground absorption and the temperature and density of the cold component are reasonable for an SNR evolving within, and mixing with, a denser medium (especially molecular gas) in the north and east.

Furthermore, two distinct Hα patterns, filamentary and diffuse, are present in the denser regions ("CN" and "C4") and the tenuous regions ("C1", "C2" and "C3"; as shown in Figure 1(b)), respectively. The [S II]/Hα ratios on the inner radio shell and on the NE limb were relatively high, ranging from 0.4 to 1.2, favoring that shock ionization occurs on the two shells and the Hα emission arises from a post-shock recombination zone (Long et al. 1991), whereas the SNR center has a low [S II]/Hα ratio (Keohane et al. 2005; Figure 3). The distinct Hα patterns and [S II]/Hα-ratios in the SNR interior compared to those along the shells imply that the optical emission in the hot remnant interior has a different origin from that on the shells (see more in Section 4.4).

4.2. *Comparision with the ROSAT, ASCA and Suzaku Results*

The X-ray spectra of the SNR interior were previously investigated by RB02 with *ROSAT* and *ASCA*, by KO05 with *ASCA* and by SK12 with *Suzaku* and some of their spectral results are summarized in Table 5. The *ROSAT* and *ASCA* observations cover the whole X-ray-emitting area, while the *Suzaku* study was toward the SNR interior. Different source (see Figure 2) and background regions are selected for spectral analysis in those studies. The background spectra of RB02 and KO05 are subtracted from the blank sky observations and a nearby source-free region (without specifying the location), respectively, while SK12 subtracted the background from a sky field ($\sim 1\overset{\circ}{.}5$ away) on the Galactic plane, respectively. In our study here, we improved on the background subtraction by adequately selecting a region as close as possible to the observation (only $\sim 30'$ away) and with the same Galactic latitude, thus minimizing any contamination by the Galactic background emission. We here compare the plasma properties determined from our *XMM-Newton* analysis with those from the previous studies.

In the studies made by RB02 and KO05, the central X-ray-emitting gas is characterized by a two-component NEI model with similar $kT_{\rm c}$ (~ 0.6 keV) and relatively high $kT_{\rm h}$ (> 1.3 keV). Nevertheless, the two studies gave inconsistent interstellar absorption and metal abundances. KO05 also extracted a spectrum in the east of their "center" region and found a smaller ratio of high-T emission measure to the low-T emission measure (~ 0.3) in the eastern region than that in the center (~ 0.5). The emission measure ratios of hot-to-cold gas in our *XMM-Newton* study (~ 0.5 in the regions "C1" and "C2"; ~ 0.3 in the area containing "C2", "C3" and "C4") are similar to those obtained by KO05. Unlike the *ASCA* and *ROSAT* studies, our *XMM-Newton* analysis based on a two-temperature model gives different values of the temperature and the ionization timescale, although we select a region ("C") in the SNR center similar to that RB02.

A discrepancy was also previously pointed out by SK12 by comparing their *Suzaku* study with the results provided by RB02: the *Suzaku* spectrum does not reveal an Fe Kα line and the central gas has much lower temperature values ($kT_{\rm c} = 0.24$ keV and $kT_{\rm h} = 0.77$ keV) when a two-temperature CIE model is used to fit the spectrum. For the *Suzaku* study, a multi-$T_{\rm z}$ recombining plasma model was preferred to describe the central gas, in order to better fit the line-like and bump-like residuals at the Si Lyα energy and in the 2.4–5.0 keV range. As noted earlier, the *Suzaku* background was carefully selected on the Galactic plane $\sim 1\overset{\circ}{.}5$ away, and thus SK12 argued that a better selection of background brought the distinguished spectroscopic results, while the *ASCA* study of KO05, which also selected a nearby background, found no evidence of over-ionization. In our *XMM-Newton* study, we have shown that the multi-T_z recombining plasma model is feasible, although not the best-fit model to explain the spectra of the central gas. However, we obtained higher electron and ionization temperatures and larger recombination timescale compared to those provided by SK12.

The spatial variations of the physical parameters found in this study indicate that a different background selection, in addition to the different spatial and spectral capabilities of the telescopes used, are the likely origin for the inconsistent results obtained by the four X-ray studies.

Furthermore, the blobby central gas as revealed by the *XMM-Newton* and *Chandra* imaging studies indicates that the X-ray emission may be contributed by more than one component, and our two-temperature thermal component model seems to be a natural explanation for this. Confirming the RRC and the recombining plasma model for the central thermal X-ray emission will require high-resolution spectra which can be obtained with the upcoming mission *ASTRO-H* (Takahashi et al. 2012).

4.3. *Non-thermal Emission from the NE Shell?*

In the northeast, the shock is propagating into dense MCs, exciting 1720 MHz OH masers, and simultaneously generating VHE γ-rays, making the remnant one of the best sites for comic ray acceleration studies. As mentioned in Section 3.3.2, an absorbed thermal+non-thermal model can reproduce the X-ray spectra of the NE shell, although the two-thermal component model is also feasible and can not be ruled out by using the currently available *XMM-Newton* data. Here, we discuss the hard non-thermal component based on the *vnei+powerlaw* model.

The hard X-ray tail in spectra of the NE shell is best fitted with a *powerlaw* model with a photon index $\Gamma = 0.9$–2.4. The unabsorbed flux of this non-thermal emission is $F_{\rm X}^{\rm NT} \sim 3.4\times10^{-13}$ erg cm^{-2} s^{-1} (0.3–5.0 keV), corresponding to a luminosity $L_{\rm X}^{\rm NT} \sim 1.6\times10^{32} d_2^2$ erg s^{-1}. There are three potential origins for the non-thermal X-rays: synchrotron emission, inverse Compton (IC) scattering, and bremsstrahlung from non-thermal electrons.

X-ray synchrotron emission has been generally detected in the fast-moving ($\gtrsim 2000$ km s^{-1}) blast waves of historical SNRs such as Cas A, *Tycho*, *Kepler*, and SN1006 (see Ballet 2006, and references therein). The electrons emitting synchrotron X-rays in the keV band requires energies over tens of TeV in a typical magnetic field ($B \approx$ 10–500μG; Vink 2012). The shock velocity in W28 measured from the optical observations is 60–100 km s^{-1} (Bohigas et al. 1983; Long et al. 1991), which is too slow to effectively accelerate the electrons to such high energies. The cut-off energy of the synchrotron emission for the shock velocity $V_{\rm s} \sim 100$ km s^{-1} is $h\nu_{\rm cut-off} = 0.56\eta^{-1}[(\chi_4 - 1/4)/\chi_4^2](V_{\rm s}/100\,{\rm km\,s^{-1}})^2$ eV (χ_4 is the compression ratio in units of 4, the deviation from Bohm diffusion $\eta \lesssim 10$; Vink 2012), which is not in the X-ray band. The synchrotron spectrum above the cut-off photon energy is thus rather steep in the X-ray band because of the quick roll over of the spectrum. Hence, the synchrotron radiation is not expected to be the dominant scenario due to the acceleration difficulty and hard spectrum. IC scattering is usually not considered to be important below 10 keV (Vink 2012), and is therefore also discarded here as the origin of the non-thermal X-ray emission.

4.3.1. *Non-thermal Bremsstrahlung*

Bremsstrahlung in the X-ray regime can be produced by suprathermal electrons of energy below several MeV. At these electron energies, Coulomb collisions dominate over other loss mechanisms, and contribute to the flattening of the spectrum and to lowering the observed flux (Sturner et al. 1997). The loss-flattened spectrum yields a hard photon index $\Gamma \approx s - 1$, where s is the spectral index of the parent electrons. Uchiyama et al. (2002) utilized this scenario to explain the extremely flat X-ray spectrum (with a photon index of $\Gamma \approx 0.8$–1.5) of several clumps in the evolved SNR γ-Cygni. A similar scenario can be applied to the case of the NE part of W28 ($\Gamma = 0.9$–2.4).

In W28, the non-thermal bremsstrahlung emitted by electrons suffering Coulomb losses is a potential explanation for the faint, relatively flat X-ray emission from the NE shell. The non-thermal electrons can be accelerated by radiative shock waves propagating into MCs (Bykov et al. 2000). If non-thermal bremsstrahlung is the dominant contributor to the hard X-ray continuum detected in the dense shell, we expect to obtain a spectral index of $s = 1.9$–3.4 for the parent elections.

4.3.2. *Secondary Leptons*

The hadronic origin of the γ-ray emission in W28 has been widely discussed and accepted. Accompanying

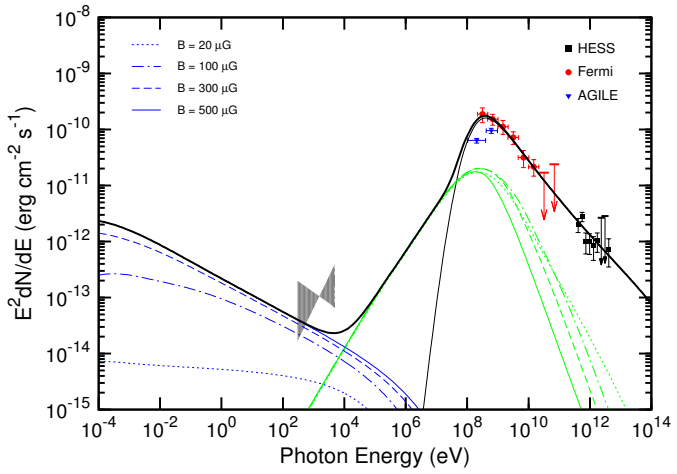

FIG. 7.— Broad-band energy spectrum (thick solid line) for a molecular cloud of mass $5 \times 10^4 M_\odot$. The observational γ-ray and non-thermal X-ray emission are indicated by dots (with error bars) and a gray bow-tie, respectively. The black solid line shows the emission from π^0-decay. Synchrotron emission and bremsstrahlung from secondary electrons are colored in blue and green, respectively. The dotted, dash-dotted, dashed, and thin solid lines refer to the emission for magnetic field values of $B_{\rm cl}$ of $20\mu G$, 100μG, $300\mu G$ and 500μG, respectively.

the π^0-decay γ-rays, secondary electrons from the decay of the charged pions can radiate non-thermal emission through the synchrotron and bremsstrahlung processes. The broadband non-thermal emission from the MCs illuminated by CRs accelerated in SNRs has been modeled by Gabici et al. (2009). We adopt this model here for W28 to calculate the broadband spectrum of the secondary electrons for the NE MCs (see Figure 7). The following parameters for W28 have been adopted in this model: age $t_{\rm age} = 4 \times 10^4$ yr, supernova explosion energy $E_{\rm SN} = 6.6 \times 10^{50}$ erg, fractional energy deposited to CRs $\eta = 0.1$, and distance of the MC to the remnant center $d_{\rm cl} \approx 10$ pc (Li & Chen 2010). The shape of the spectrum is mainly determined by four parameters: the correction factor of the diffusion coefficient (χ), the power-law index of diffusion coefficient (δ), the magnetic field in the MC ($B_{\rm cl}$), and the cloud mass ($M_{\rm cl}$). We initially determine the distribution of the secondary electrons by fitting the γ-ray data from the *Fermi* (Abdo et al. 2010) and H.E.S.S. (Aharonian et al. 2008) observations. The fitting gives $\chi = 0.08$, $\delta = 0.45$ and $M_{\rm cl} = 5 \times 10^4 M_\odot$ which are consistent with the previous results obtained by Li & Chen (2010).

The synchrotron radiation from the secondary electrons strongly depends on the strength of the magnetic field in the MC and gets enhanced with increasing magnetic field values. However, even if the magnetic field is increased up to 500 μG, the synchrotron emission is not strong enough to explain the observed non-thermal X-rays. Moreover, the bremsstrahlung from the secondary electrons, which peaks around 100 MeV, is also too low to fit the observed X-ray data. The emissivity of bremsstrahlung from the secondary electrons is proportional to the gas density squared but not sensitive to the magnetic field. Increasing the gas density, however, does not enhance the flux due to the electrons' strong energy loss by bremsstrahlung. The spectrum extraction region "Shell" in the NE edge just overlaps a small part of the illuminated MC; however, the observed non-thermal X-ray flux is still much higher than could be produced by the secondary electrons from the whole MC. In summary, the secondary electrons' origin is not a favorable scenario to explain the hard X-ray tail.

4.3.3. *Radio Emission and Non-thermal Bremsstrahlung X-rays*

It is of interest to search for the relationship between the non-thermal X-rays and the radio synchrotron emission, since the bright X-ray shell appears spatially coincides with the radio peak. It is suggested that, in an inhomogeneous medium, the fast shock propagating in the intercloud medium accelerates particles to higher energies and generates radio synchrotron and γ-ray emission, while the shock propagating in the clouds is able to accelerate electrons to energies below GeV giving birth to non-thermal hard X-ray and MeV γ-ray emission (Bykov et al. 2000; Chevalier 1999).

The overall radio spectral index of W28 is observed to be $\alpha \sim 0.35$ ($S \propto \nu^{-\alpha}$), with the index values on the bright radio filaments systematically flatter than in the SNR cavity (Dubner et al. 2000). Accordingly, we infer the energy spectral index of the radio emitting electrons on the shell to be $s < 1.7$, which is much lower than the index of the parent electrons radiating bremsstrahlung X-rays ($s = 1.9$–3.4; see Section 4.3.1 above).

This discrepancy implies that non-thermal radio and X-ray emission do not arise from the same population of electrons, and suggest that the radio emission likely originates from the intercloud shock while the flat X-ray emission is associated with the cloud shock.

4.4. *The SNR Interior Gas*

As discussed in Sections 4.1 and 4.2, the gas in the interior of W28 is spatially variant, clumpy, X-ray bright, and best characterized by a two-temperature plasma, or even a recombining plasma. In Sections 4.4.1 and 4.4.2, we discuss the physics of the centrally bright X-ray emission based on the former and latter models, respectively.

4.4.1. *Physics of the Central Thermal X-Ray Emission*

Projection effect is one of the mechanisms that is suggested to explain the centrally peaked X-ray morphology. One projection case occurs when the interaction zone between the SNR and a one-sided dense medium is projected, along the line of sight, to the remnant interior (Petruk 2001). The enhanced intervening hydrogen absorption, high [S II]/Hα ratio, low temperature, and relatively high density along the northern inner shell (typified by region "CN") indeed imply that a shock interaction with dense interstellar medium (most probably, MC) is projectively seen in the interior. Although the X-ray brightness seems to peak inside the inner shell, we do not attribute it to the projection effect; the reason is that the scenario that the bright X-rays come from the shocked dense gas in the remnant's edge is inconsistent with the low [S II]/Hα ratio near the X-ray brightness peak. Another type of projection effect was studied by Shimizu et al. (2012): When the shock breaks out of disk-like circumstellar medium to a rarefied interstellar medium, the hot over-ionized plasma appears

to be centrally-filled (bar-like) in the equatorial plane. The scenario was applied to describe the X-ray morphology of the much younger SNR W49B (1000–4000 yr; see Shimizu et al. 2012, and references therein; see also Zhou et al. 2011). However, at the late-phase ($> 10,000$ yr), the SNR evolves to be shell-like independently of the viewing angle rather than centrally-filled, and W28, at a large age (3–4×10^4 yr), would be of this case. Hence, the projection effects are unlikely to explain the central X-ray emission.

The thermal conduction model is often used to explain the central X-ray emission of MM SNRs (Cox et al. 1999; Shelton et al. 1999). Without the suppression of magnetic fields, the conduction timescale is given by $t_{\rm cond} \approx k n_e l_T^2/\kappa \sim 56 (n_e/1\ {\rm cm}^{-3}) (l_T/10\,{\rm pc}) (kT/0.6\,{\rm keV})^{-5/2} (\ln\Lambda/32)$ kyr, where l_T ($= T_e/|\nabla T_e|$) is the scale length of the temperature gradient, κ is the collisional conductivity, and $\ln\Lambda$ is the Coulomb logarithm. If l_T is taken as the radius of the SNR ~ 10 pc in the northern hemisphere, and we use the temperature 0.77 keV and density 0.69 cm^{-3} of the hot component in the central region "C", the conduction timescale is estimated to be 21 kyr, which is smaller than the dynamical age of W28. Hence, thermal conduction may play a role in the center of W28. However, the almost monotonic decrease of the temperature of both the hot and cold components from west to east across the central region (see Section 4.1.3 and Table 4) is inconsistent with the prediction of the thermal conduction model. Actually, RB02 have also regarded a large temperature gradient (observed with *ROSAT* and *ASCA*) from the western ear-like structure to the eastern shell as a difficulty for the model to be applied to W28. Moreover, in the thermal conduction model, the pressure at the SNR center is ~ 0.3 of that at the shell and the central density is much lower (~ 0.13 at radiative shell formation) than the ambient gas density; but in this study, the pressure ratio between the central gas and the NE shell is ~ 0.7 and the density ratio is $\gtrsim 0.26$, which are much larger than the model prediction. These inconsistencies may be due to the over-simplified conduction model in comparison with a more complicated, highly nonuniform, interstellar environment and physical conditions. Also, the magnetic field may be another potential factor to suppress the effect of thermal conduction.

An alternative scenario for the centrally brightened X-ray morphology is the cloudlet evaporation model (White & Long 1991). A series of observational facts in W28 seem to favor this scenario. Firstly, blobby X-rays and diffuse Hα emission are detected in the SNR center, indicating that the central gas is highly clumpy and thus probably contains plenty of cloudlets required by the model. Secondly, the cloudlets embedded in a previously shocked, hot gas are gradually evaporated, and the newly evaporated material is expected to be dense and characterized by a low temperature plasma. This can naturally explain the two-temperature component model of the X-ray emission from the W28 interior. Thirdly, the cold component in our best fit spectral model has a low ionization timescale ($\sim 4 \times 10^{11}$ cm^{-3} s) indicating an NEI state, and this is expected by the cloudlet evaporation model. Moreover, the cloudlet evaporation model predicts that collisionally excited Hα emission is generated in the evaporating flow and has a larger luminosity than the X-ray luminosity for evaporation-dominated SNRs, and this has indeed been pointed out to be the case in W28 (Long et al. 1991).

Comparatively, the cloudlet evaporation mechanism can essentially explain the properties of the X-ray emission in the central region of W28, but the thermal conduction mechanism can also play a role in a length scale comparable to the remnant's radius. However, the limited field of view in the *XMM-Newton* observations and the complicated X-ray brightness profile that RB02 obtained using *ROSAT* observation prevent us from a detailed quantitative calculation using the evaporation model.

4.4.2. *Relation to the Recombining Plasma?*

The recombining plasma model is also a feasible model for the central gas (see Section 4.1.2). The presence of the over-ionized plasma needs a rapid cooling process, such as drastic adiabatic expansion (including rarefaction process, Itoh & Masai 1989), thermal conduction (Kawasaki et al. 2002) and both processes (Zhou et al. 2011). The rarefaction scenario predicts a rapid electron cooling after the shock breaking out of the dense circumstellar medium and adiabatically expands to a tenuous ambient medium. Though, the slight density variation inferred from the *XMM-Newton* analysis seems not support a distinctive density decrease from the explosion center. Thermal conduction to low-temperature gas in small clouds may also rapidly cool the nearby hot gas. As diffuse Hα emission has been detected in the SNR center and overlaps the hot X-ray-emitting plasma, it can be expected that many dense clouds emitting the optical emission are embedded in the hot plasma. On the other hand, if cloudlet evaporation is not negligible, it is very possible that the hot plasma could be rapidly cooled down by mixing with the dense and cooler plasma evaporated from the clouds. Indeed, a numerical simulation by Zhou et al. (2011) has shown that the mixing of the gas evaporated from dense material is one important cooling mechanism to produce the over-ionized plasma in SNR W49B.

5. SUMMARY

We have investigated the hot gas in the northern hemisphere of the MM SNR W28 by performing an *XMM-Newton* imaging and spatially resolved spectroscopic study. The main results and conclusions are summarized as follows:

1. The *XMM-Newton* image reveals a deformed shell in the northeast which partly overlaps the molecular gas and Hα emission. The X-ray emission in the interior is blobby and appears to be confined in the north and east by the Hα filaments.

2. The X-rays arising from the NE shell, where the shock–MC interaction is evident and γ-ray emission is seen, consist of a soft thermal component (~ 0.3 keV) plus a hard component of either non-thermal ($\Gamma = 0.9$–2.4) or thermal ($kT_{\rm h} \sim 0.6$ keV) origin. The ionization age is estimated to be $> 0.75 \times 10^4$ yr and 1–4×10^4 yr, respectively, from the former model (*vnei+powerlaw*) and the hot component

of the latter model (double-*vnei*), further supporting an evolved stage of SNR W28. According to the *vnei+powerlaw* model, we estimate a density of $\sim 2.7\,\mathrm{cm}^{-3}$ for the hot post-shock plasma. In the double-*vnei* model, the soft X-ray component may originate in the shocked cloud material with a density of $\sim 2.5\,\mathrm{cm}^{-3}$, while the harder X-rays may be emitted from the inter-cloud gas with a density of $\sim 1.2\,\mathrm{cm}^{-3}$.

3. If the hard X-ray emission of the NE shell is indeed non-thermal, a possible origin for its flat spectrum is the non-thermal bremsstrahlung emitted by the electrons suffering Coulomb losses. The low spectral index and the difficulty in accelerating electrons to >TeV-energy disfavor a synchrotron origin. The hard spectrum also cannot be reproduced by the secondary electrons from the hadronic interaction between the cosmic ray protons and the ambient MCs. Furthermore, the spectral index of the parent electrons of the non-thermal X-rays ($s = 1.9$–3.4), is larger than the index of the electrons generating the synchrotron radio emission ($s < 1.7$), indicating that the X-ray and radio emission do not share the same population of electrons and possibly originate from different shocks.

4. The gas inside the remnant yields a low elemental abundance with no evidence of ejecta. Following a careful background subtraction that minimizes contamination by the Galactic ridge emission (an improvement over previous X-ray studies), we find that the spectra of the hot central gas can be best fitted with a two-temperature model (*vnei+vmekal*) and also can be adequately described with a recombining plasma model (*neij*).

5. In the two-temperature model (for the central gas), the cold component is under-ionized at a temperature ~ 0.4 keV, and the hot component is a CIE plasma at ~ 0.8 keV. The spatially resolved spectral study reveals variations in temperature, gas density, and intervening absorption inside the remnant. In the north and east ("CN" and "C4") of the X-ray-brightness peak, the plasma gets relatively cold and dense, and the X-rays suffer heavier foreground absorption than those in other parts of the central region, and filamentary Hα structures are detected. This distribution is consistent with the scenario that the remnant is evolving in an non-uniform medium with dense gas located in the northeast.

6. The hot central gas can alternatively be described with a multi-T_z recombining plasma model with an electron temperature ~ 0.6 keV. The recombination age of the gas is estimated as $\sim 2.9 \times 10^4$ yr, slightly lower but close to the dynamical age of W28 (3–4×10^4 yr). The parameters of the recombination model show a slight variation among the small regions in the SNR interior, except that the northern region "CN", spatially coincident with the inner radio shell, shows the largest recombination timescale and lowest ionization temperature.
7. The clumpy structure of the central hot gas revealed by the X-ray mapping favors the cloudlet evaporation process, which can explain the two-temperature components, the low ionization timescale of the cold component, and the larger Hα luminosity than that of the X-ray. Though, in the two-temperature model, thermal conduction may also play a role in a scale as large as the remnant's radius. *ASTRO-H* will help confirm the physical mechanism at play in this, and other, MM SNRs.

Note added in manuscript. While this paper was under revision, Nakamura et al. (2014) posted on the arXiv a paper studying the NE shell of W28 with *XMM-Newton* observations. There are some differences between our results and theirs. We conclude that a two-component is required for the NE shell but their fit with a single thermal component with $kT \sim 0.3$ keV is satisfactory. The possible discrepancy between our results may be due to the different background selection. They selected a background region inside the SNR where X-ray emission is clearly seen (see their Figure 3(a)). We note that an additional hard component was previously pointed out by Ueno et al. (2003), which is consistent with our finding.

We gratefully acknowledge the anonymous referee for valuable comments. We are thankful to Ken Tatematsu for providing us with the calibrated JCMT CO data. We also thank Hui Li and Xin Zhou for helpful discussions. We acknowledge the support from the Natural Sciences and Engineering Research Council of Canada (NSERC), the 973 Program grant 2009CB824800, the NSFC grant 11233001, the Chinese Scholarship Council, the grant 20120091110048 from the Educational Ministry of China, the Canada Research Chairs program and the Canadian Space Agency.

REFERENCES

Abdo, A. A., Ackermann, M., Ajello, M., et al. 2009, ApJ, 706, L1
Abdo, A. A., Ackermann, M., Ajello, M., et al. 2010b, ApJ, 718, 348
Aharonian, F., Akhperjanian, A. G., Bazer-Bachi, A. R., et al. 2008, A&A, 481, 401
Arikawa, Y., Tatematsu, K., Sekimoto, Y., & Takahashi, T. 1999, PASJ, 51, L7
Audard, M., Behar, E., Güdel, M., et al. 2001, A&A, 365, L329
Ballet, J. 2006, Advances in Space Research, 37, 1902
Bocchino, F., Maggio, A., & Sciortino, S. 1999, A&A, 342, 839
Bohigas, J., Ruiz, M. T., Carrasco, L., Salas, L., & Herrera, M. A. 1983, RMxAA, 8, 155
Brandt, T., & Fermi LAT Collaboration 2012, American Astronomical Society Meeting Abstracts #219, 219, #213.03
Brickhouse, N. S., Dupree, A. K., Edgar, R. J., et al. 2000, ApJ, 530, 387
Bykov, A. M., Chevalier, R. A., Ellison, D. C., & Uvarov, Y. A. 2000, ApJ, 538, 203
Chevalier, R. A. 1999, ApJ, 511, 798
Claussen, M. J., Frail, D. A., Goss, W. M., & Gaume, R. A. 1997, ApJ, 489, 143
Cox, D. P., Shelton, R. L., Maciejewski, W., et al. 1999, ApJ, 524, 179
Cui, W., & Cox, D. P. 1992, ApJ, 401, 206
Dubner, G. M., Velázquez, P. F., Goss, W. M., & Holdaway, M. A. 2000, AJ, 120, 1933
Frail, D. A., Goss, W. M., & Slysh, V. I. 1994, ApJ, 424, L111
Frail, D. A. 2011, Mem. Soc. Astron. Italiana, 82, 703

Ferrand, G., & Safi-Harb, S. 2012, Advances in Space Research, 49, 1313
Gabici, S., Aharonian, F. A., & Casanova, S. 2009, MNRAS, 396, 1629
Giuliani, A., Tavani, M., Bulgarelli, A., et al. 2010, A&A, 516, L11
Goudis, C. 1976, Ap&SS, 40, 91
Green, A. J., Frail, D. A., Goss, W. M., & Otrupcek, R. 1997, AJ, 114, 2058
Hartman, R. C., Bertsch, D. L., Bloom, S. D., et al. 1999, ApJS, 123, 79
Hewitt, J. W., Yusef-Zadeh, F., & Wardle, M. 2009, ApJ, 706, L270
Hewitt, J. W., & Fermi LAT Collaboration 2012, American Astronomical Society Meeting Abstracts #219, 219, #239.23
Ilovaisky, S. A., & Lequeux, J. 1972, A&A, 18, 169
Itoh, H., & Masai, K. 1989, MNRAS, 236, 885
Jiang, B., Chen, Y., Wang, J., et al. 2010, ApJ, 712, 1147
Jones, T. W., Rudnick, L., Jun, B.-I., et al. 1998, PASP, 110, 125
Kaastra, J. S., Mewe, R., & Nieuwenhuijzen, H. 1996, UV and X-ray Spectroscopy of Astrophysical and Laboratory Plasmas, ed. K. Yamashita & T. Watanabe (Tokyo: Universal Academy Press), 411
Kawasaki, M. T., Ozaki, M., Nagase, F., et al. 2002, ApJ, 572, 897
Kawasaki, M., Ozaki, M., Nagase, F., Inoue, H., & Petre, R. 2005, ApJ, 631, 935 (KO05)
Keohane, J. W., Rho, J., Pannuti, T. G., Borkowski, K. J., & Winklery, P. F. 2005, X-Ray and Radio Connections,
Li, H., & Chen, Y. 2010, MNRAS, 409, L35
Li, H., & Chen, Y. 2012, MNRAS, 421, 935
Long, K. S., Blair, W. P., Matsui, Y., & White, R. L. 1991, ApJ, 373, 567
Miceli, M., Reale, F., Orlando, S., & Bocchino, F. 2006, A&A, 458, 213
Morrison, R., & McCammon, D. 1983, ApJ, 270, 119
Nakamura, R., Bamba, A., Ishida, M., et al. 2014, PASJ, 66, 62
Nicholas, B. P., Rowell, G., Burton, M. G., et al. 2012, MNRAS, 419, 251
Ohira, Y., Murase, K., & Yamazaki, R. 2011, MNRAS, 410, 1577
Ohnishi, T., Koyama, K., Tsuru, T. G., et al. 2011, PASJ, 63, 527
Ozawa, M., Koyama, K., Yamaguchi, H., Masai, K., & Tamagawa, T. 2009, ApJ, 706, L71
Parker, Q. A., Phillipps, S., Pierce, M. J., et al. 2005, MNRAS, 362, 689
Petruk, O. 2001, A&A, 371, 267
Pollock, A. M. T. 1985, A&A, 150, 339
Reach, W. T., Rho, J., & Jarrett, T. H. 2005, ApJ, 618, 297
Rho, J., & Borkowski, K. J. 2002, ApJ, 575, 201 (RB02)
Rho, J., & Petre, R. 1998, ApJ, 503, L167
Sawada, M., & Koyama, K. 2012, PASJ, 64, 81 (SK12)
Sedov, L. I. 1959, Similarity and Dimensional Methods in Mechanics, New York: Academic Press, 1959,
Shelton, R. L., Cox, D. P., Maciejewski, W., et al. 1999, ApJ, 524, 192
Shimizu, T., Masai, K., & Koyama, K. 2012, PASJ, 64, 24
Smith, R. K., & Hughes, J. P. 2010, ApJ, 718, 583
Sturner, S. J., & Dermer, C. D. 1995, A&A, 293, L17
Sturner, S. J., Skibo, J. G., Dermer, C. D., & Mattox, J. R. 1997, ApJ, 490, 619
Strüder, L., Briel, U., Dennerl, K., et al. 2001, A&A, 365, L18
Takahashi, T., Mitsuda, K., Kelley, R., et al. 2012, Proc. SPIE, 8443
Turner, M. J. L., Abbey, A., Arnaud, M., et al. 2001, A&A, 365, L27
Uchiyama, Y., Takahashi, T., Aharonian, F. A., & Mattox, J. R. 2002, ApJ, 571, 866
Ueno, M., Bamba, A., & Koyama, K. 2003, International Cosmic Ray Conference, 4, 2401
Velázquez, P. F., Dubner, G. M., Goss, W. M., & Green, A. J. 2002, AJ, 124, 2145
Vink, J. 2012, A&A Rev., 20, 49
Wang, Q. D., Chaves, T., & Irwin, J. A. 2003, ApJ, 598, 969
White, R. L., & Long, K. S. 1991, ApJ, 373, 543
Wootten, A. 1981, ApJ, 245, 105
Yamaguchi, H., Ozawa, M., Koyama, K., et al. 2009, ApJ, 705, L6
Yan, H., Lazarian, A., & Schlickeiser, R. 2012, ApJ, 745, 140
Yusef-Zadeh, F., Wardle, M., Rho, J., & Sakano, M. 2003, ApJ, 585, 319
Zhou, X., Bocchino, F., Miceli, M., Orlando, S., & Chen, Y. 2010, MNRAS, 406, 223
Zhou, X., Miceli, M., Bocchino, F., Orlando, S., & Chen, Y. 2011, MNRAS, 415, 244